공학박사 학위논문

Wavepath analysis and strategies for waveform inversion in the Laplace domain

라플라스 영역에서의 파동경로 분석과 이에 따른 파형역산의 전략

2017 년 8 월

서울대학교 대학원

에너지시스템공학부

권 정 민

Abstract

Wavepath analysis and strategies for waveform inversion in the Laplace domain

Jungmin Kwon

Department of Energy Systems Engineering

The Graduate School

Seoul National University

Laplace-domain waveform inversion (WI) is a technique for estimating long wavelength velocity models. The velocity model, estimated by Laplace-domain WI, is used as an initial velocity model for techniques such as frequency-domain and time-domain waveform inversion. These techniques are then used to develop high resolution velocity models used in subsurface imaging. Since frequency-domain and time-domain waveform inversion are sensitive to the initial velocity model, model resolution of Laplace-domain WI is an important factor in the overall velocity-estimation process. In addition, since the cost for obtaining the wavefield of the Laplace domain is large, it is necessary to improve the convergence rate and efficiency of Laplace-domain WI. Previous Laplace-domain WI studies have shown difficulty in analyzing model resolution and convergence rate due to insufficient understanding of the wavepath and its role in representing the relationship between the model

parameters and seismic data. This study investigates the characteristics of the wavepath in the Laplace domain which have not been clarified in previous research. Through this study, we implement convergence rate, model resolution, and efficiency analysis for Laplace-domain inversion. By introducing the attenuation constant, which can be considered a Laplace constant in the spatial domain, we prove that the wavepath of the Laplace domain is a real exponential basis with the product of the attenuation constant vector and the position vector as an exponent. We also prove that the attenuation constant vector is a function of both the Laplace constant and the incident angle. From the numerical example, it can be confirmed that the attenuation constant depends on both the Laplace constant and the incident angle. In addition, this study shows that it is reasonable to apply the Gauss-Newton method to Laplace-domain WI for fast convergence. The wavepath of the Laplace domain is a real exponential function, which has a large condition number. The numerical example of the BP benchmark model demonstrates the effectiveness of the Gauss-Newton method in this Laplace-domain WI algorithm. We also prove that a wide range of incident angles is essential to obtain a high resolution model through Laplace-domain inversion. The relationship between the model resolution and the incident angle range explains why the model resolution decreases as the offset-depth ratio increases. Also, horizontal and vertical resolution changes, depending on the exploration environment, can be predicted. Finally, we propose an efficient Laplace constant selection strategy to improve the efficiency of Laplace domain inversion. The Laplace constants selected through the proposed method improve efficiency by maintaining continuity of the range of attenuation constants and by minimizing unnecessary repetition of attenuation constants. From the numerical example, it can be seen that the proposed Laplace constant selection strategy yields superior results in terms of both efficiency and accuracy, compared with the strategy of choosing Laplace

constants at fixed intervals. This applies for both the simple-model and complex-model case, such as the SEG/EAGE salt dome model.

Keywords : Laplace-domain waveform inversion, Wavepath, Gauss-Newton method, Model resolution, Laplace constant selection

Student Number : 2013-21005

Contents

List of Figures

List of Tables

List of Algorithms

Chapter 1 Introduction

1.1 Background

Accurate velocity estimation is an essential process for successfully imaging oil and gas reservoirs. Velocity analysis using semblance or traveltime tomography has conventionally been used in velocity estimation. However, these methods provide low-resolution results because the information they use from seismograms is limited. Many studies have been conducted to delineate subsurface velocity models from seismic data with high resolution. One such technique which is actively studied is Full waveform inversion (FWI). FWI provides a high-resolution velocity model because it uses all waveforms (Tarantola, 1984, 1986; Pratt et al., 1998; Shin and Cha, 2008, 2009; Virieux and Operto, 2009; van Leeuwen and Herrmann, 2013; Warner et al., 2013; Vigh et al., 2014).

Among them, frequency-domain waveform inversion (WI) is known as a very efficient algorithm for constructing velocity models. It has been observed that the frequency-domain WI algorithm provides an unaliased model image with only a limited number of frequencies (Pratt and Worthington, 1988; Liao and McMechan, 1996; Forgues et al., 1998). This hypothesis was proved by the analysis, proposed by Wu and Toksöz (1987), which shows that a finite range of wavenumbers of the model can be obtained with only a single frequency. Given that the number of frequencies is proportional to the computational cost, the fact that frequency-domain WI can build a reasonable model using a small number of frequencies implies that it is an efficient algorithm for velocity estimation.

Sirgue and Pratt (2004) provided instructions on how to choose a set of frequencies for efficient implementation of frequency-domain WI. This method helps to select a set of frequencies that maintain the continuity of the wavenumber (Woodward, 1992) and minimize the redundancy of the wavenumber for a given source-receiver geometry. They verified that the larger the range of offsets, the fewer frequencies are required in frequency-domain WI. This frequency selection strategy makes the implementation of the frequency-domain WI algorithm more efficient.

On the other hand, frequency-domain WI has ill conditioned characteristics which leads to slow convergence. Therefore, research has been conducted to improve the convergence rate of frequency-domain WI. As a representative example, Pratt et al. (1998) proposed frequency-domain WI using Gauss-Newton method, which is a nonlinear optimization scheme considering the Hessian matrix. According to Press et al. (1992) and Strutz (2016), the gradient descent method has an extremely slow convergence rate if the problem is ill-conditioned. The Gauss-Newton method overcomes these shortcomings and converges with far fewer iterations than the gradient descent method.

However, the Gauss-Newton method requires a lot of computational cost for constructing and solving the Hessian matrix, which is a dense matrix. Métivier et al. (2013) solved this computational cost problem using a truncated Gauss-Newton method which adopts the conjugate gradient (CG) method. The truncated Gauss-Newton method is an efficient method in that it can be applied without constructing the Hessian matrix and can solve the Hessian matrix by repeating matrix-vector multiplications without a matrix inverse. By using the truncated Gauss-Newton method, the frequency-domain WI algorithm can overcome this convergence rate issue.

There is another limitation in frequency-domain WI which must be addressed.

The frequency-domain WI algorithm, can easily reach a local minima; thereby generating poor-quality velocity models is highly likely because of the nonlinear nature of the inverse problems. To overcome this limitation of the frequency-domain WI algorithm, seismic data should contain low-frequency components or the initial model that is used for the inverse problem should be sufficiently close to the true velocity model.

Until recently, many studies have focused on designing inversion algorithms to generate good initial models for FWI. One of the algorithms used to generate initial models, specifically, ray-based refraction traveltime tomography, has been studied by many geophysicists (Hampson & Russell 1984; Schneider & Kuo 1985; White 1989; Zhu & McMechan 1989; Docherty 1992; Qin et al. 1993; Cai & Qin 1994; Stefani 1995; Shtivelman 1996; Zhang & Toksöz 1998). This algorithm provides limited information on the subsurface velocity model because of its difficulty in handling diffraction (Wu & Toksöz 1987; Woodward 1992; Zelt & Barton 1998). Pyun et al. (2005) developed a first-arrival traveltime tomography algorithm, using the damped monochromatic wave equation proposed by Shin et al. (2003) which can overcome some of the limitations of ray-based refraction traveltime tomography.

Other methods of building initial models for FWI have been studied (Brenders et al. 2008; Sirgue et al. 2009; Plessix et al. 2010; Bozdağ et al. 2011; Choi & Alkhalifah 2013; Fichtner et al. 2013; Chi et al. 2014; Datta & Sen 2016). Bharadwaj et al. (2013) proposed an FWI method that used two different functions. A velocity model was generated from an inversion using a cross-correlation-based misfit function, then another inversion using the classic least-squares objective function was used to exploit this output velocity model as an input. Similarly, Xu et al. (2012) used cross-correlation between the calculated and observed data as a cost function, but these authors used reflections to

reconstruct the long-wavelength components of the model. They used cross-correlation-related objective functions to take advantage of phase information in data and obtain a long-wavelength background velocity model. Bozdağ et al. (2011) employed a Hilbert transform to construct a misfit function without the interaction of phase and amplitude information.

There have been other studies for overcoming local minima. Sava and Biodndi (2004a, b) suggested wave-equation migration velocity analysis (WEMVA) which inverts the velocity model using migrated images. This does not require as close of an initial model as conventional FWI does to mitigate the cycle-skipping problem. Ratcliffe et al. (2011) utilized deconvolution to extract low-frequency components for their waveform inversion. Alkhalifah and Choi (2012) used objective functions based on the unwrapped phase, and Ma and Hale (2013) suggested an algorithm to estimate time shifts between recorded data and synthetic data using dynamic image warping. Recently, Warner and Guasch (2014) suggested an 'adaptive waveform inversion (AWI)', which adopts a correlation-based objective function as a solution for the cycle-skipping problem.

Among the algorithms for generating initial models, the Laplace-domain waveform inversion (WI), which is suggested by Shin and Cha (2008), is well-known as an effective method for generating starting models. The Laplace-domain WI algorithm uses Laplace-transformed wavefields to estimate velocity models. The Laplace-domain has the advantage that there are fewer local minima in the objective function compared to frequency-domain WI (Shin and Ha, 2008).

Additional studies on the appropriate objective function for Laplace-domain WI have been actively conducted (Shin and Ha, 2008; Park et al., 2013; Jun et al., 2016). Laplace-domain wavefields have the property of exponentially

decreasing magnitude as distance increases. Therefore, far offset information of seismic data can be reflected well only when we use an objective function compensating for amplitude loss due to increased offset. The logarithmic objective function is a typical example of the proper objective function for Laplace-domain WI, and is most popularly used for it.

In spite of these various studies, the field of Laplace-domain WI still has room for improvement. Ha and Shin (2013) proved that Laplace-domain WI has a disadvantage in that the inverted model with high resolution cannot be obtained using only the gradient descent method. However, this resolution problem of the gradient descent method has yet to be addressed in any previous studies.

Also, studies on the relationship of Laplace constant, experimental setup and target position with model resolution are still insufficient. Bae et al. (2012) observed how the depth penetration varies with the Laplace constant and offset in Laplace-domain inversion. If the Laplace constant is very large, Laplace-domain WI can be approximated by refraction tomography (Pyun et al., 2005), which is only able to invert shallow areas. Deeper locations can be estimated as the Laplace constant decreases. This paper also confirmed, along with Ha et al. (2012), that depth penetration increases with maximum offset in this paper. However, only the analysis using depth penetration alone had a limitation in fully explaining the model resolutions of various exploration environments.

Moreover, proper selection of Laplace constants requires additional studies. Park et al. (2010) has proposed a strategy for determining the maximum and minimum values of the Laplace constant considering numerical error and depth penetration. However, it does not provide a guideline on how Laplace constants should be chosen between arbitrary upper and lower bounds of Laplace constants.

1.2 Motivation and research objective

Although there have been many studies on the Laplace-domain WI, it still has more unanswered questions than frequency-domain WI as discussed in Chapter 1.1. First, the gradient descent method is still used instead of the Gauss-Newton method. This has already proven to have a higher convergence rate in the Laplace-domain WI, and there has been no research to accelerate the convergence rate of it. In addition, there are only empirical observations on how the model resolution is determined in Laplace-domain WI. Moreover, while there is a guideline on how to choose the frequencies in frequency-domain WI, the criteria for choosing the Laplace constant is uncertain in Laplace-domain WI.

The reason why these questions in Laplace-domain WI have not been solved yet is that the characteristics of the wavepath of the Laplace domain have not yet been determined. The wavepath, also known as data kernel, defines the relationship between the data domain and the model domain. Thus, the identification of this wavepath is fundamental to understanding the characteristics of the inversion algorithm that estimate the model parameters from the data. Frequency-domain WI is a representative example of this. By analyzing the characteristics of the Born wavepath in frequency-domain WI, the theoretical background of the analysis of the Hessian matrix of the frequency domain, analysis of model resolution, and frequency selection method may be established. Therefore, the wavepath of the Laplace domain needs to be well investigated to properly analyze Laplace-domain WI.

This paper aims at grasping the wavepath of the Laplace-domain and solving many questions about Laplace-domain WI that have not been solved in

previous studies. This paper focuses specifically on explaining (1) the necessity of the Gauss-Newton method, (2) model resolution depending on the scattering angle and Laplace constant and finally (3) an efficient guideline for Laplace constant selection.

1.3 Outline

First, in Chapter 2, we briefly review the wave equation in the Laplace domain and the logarithmic objective function which is most commonly used for Laplace-domain WI. We then show that the wavepath in the Laplace domain is a linear operator consisting of real exponentially decaying bases, using both the concept of an attenuation constant, which can be defined as the Laplace constant for the space domain, and the Laplace-domain Green's function assuming a homogeneous acoustic medium.

In Chapter 3, using the characteristics of the wavepath in the Laplace domain, we find that the inverse problem using the Laplace-domain wavefields an ill-conditioned problem. Because of this ill-conditioning, fast convergence cannot be guaranteed with the gradient descent method, and it is desirable to use the Gauss-Newton method for fast convergence in the Laplace-domain WI algorithm. The numerical example using the BP benchmark model confirms the superiority of the Gauss-Newton method for Laplace-domain WI by comparing the results of the Gauss-Newton method and the gradient descent method.

Moreover, in Chapter 4, we verify that model resolution of Laplace-domain WI is dependent on the condition number of the Laplace-domain wavepath when there are numerical errors. By clarifying the relationship between the condition number of the Laplace domain and the range of the attenuation constant, which depends on a scattering angle, we confirm that the model resolution decreases as the scattering angle becomes narrower. Based on the above analysis, numerical examples show how the model resolution changes depending on the offset-depth ratio and type of experimental setup.

In Chapter 5, finally, we propose an efficient strategy for selecting Laplace

constants for Laplace-domain WI. Chapter 5 explains why it is important that the range of vertical attenuation constants is both continuous and not overlapping as much as possible, and how to achieve these two conditions. We also show how to compensate for the effects of geometrical spreading in the proposed strategy. Furthermore, we discuss whether this strategy is also effective in 2D or 3D heterogeneous media. A numerical example shows how the proposed method outperforms the conventional Laplace constant selection method.

Chapter 2 Wavepath in the Laplace domain

This chapter aims to clarify the wavepath of Laplace-domain WI, which is usually used with the logarithmic objective function. First, the Laplace-domain Green's function is introduced, and how the Green's function of the Laplace domain can be expressed in a homogeneous acoustic unbounded medium. Using the Green’s function of the Laplace domain, we derive that the Rytov wavepath, which means the wavepath of the logarithmic objective function, of the Laplace domain can be approximated to a real exponentially decaying basis. We also prove that its exponent is the product of the space vector and the scattering attenuation constant, which means the damping constant in the spatial domain.

2.1 Wave equation in the Laplace domain

First, we briefly review the wave equation in the Laplace domain (Shin and Cha, 2008). The acoustic wave equation in the time-domain can be expressed as

$$\frac{1}{c(\mathbf{x})^2}\frac{\partial^2 \tilde{u}(\mathbf{x}|\mathbf{s},t)}{\partial t^2} - \nabla^2 \tilde{u}(\mathbf{x}|\mathbf{s},t) = \tilde{w}(t)\delta(\mathbf{x}-\mathbf{s}), \tag{2.1.1}$$

where $c(\mathbf{x})$ is the P-wave velocity at a position $\mathbf{x}$ and $\tilde{u}(\mathbf{x}|\mathbf{s},t)$ is the acoustic wavefield propagated from the source position $\mathbf{s}$ observed at position $\mathbf{x}$ and time t. $\tilde{w}(t)$ is a time-domain source wavelet. The wave equation in the Laplace domain can be obtained by applying the Laplace transform to Equation (2.1.1) as follows:

$$\frac{\sigma^2}{c(\mathbf{x})^2}u(\mathbf{x}|\mathbf{s},\sigma) - \nabla^2 u(\mathbf{x}|\mathbf{s},\sigma) = w(\sigma)\delta(\mathbf{x}-\mathbf{s}), \tag{2.1.2}$$

where

$$\begin{aligned} u(\mathbf{x}|\mathbf{s},\sigma) &= \int_0^\infty \tilde{u}(\mathbf{x}|\mathbf{s},t)\exp(-\sigma t)dt, \\ w(\sigma) &= \int_0^\infty \tilde{w}(t)\exp(-\sigma t)dt, \end{aligned} \tag{2.1.3}$$

and σ is a Laplace constant. $u(\mathbf{x}|\mathbf{s},\sigma)$ is called a Laplace-domain wavefield. The Laplace-domain wavefield can be expressed as a product of a *Green's function* $g(\mathbf{x}|\mathbf{s},\sigma)$ and the source wavelet in the Laplace domain $w(\sigma)$ as follows:

$$u(\mathbf{x}|\mathbf{s},\sigma) = w(\sigma)g(\mathbf{x}|\mathbf{s},\sigma), \tag{2.1.4}$$

where

$$\frac{\sigma^2}{c(\mathbf{x})^2} g(\mathbf{x}|\mathbf{s},\sigma) - \nabla^2 g(\mathbf{x}|\mathbf{s},\sigma) = \delta(\mathbf{x}-\mathbf{s}). \quad (2.1.5)$$

Through discretization using the finite difference method or finite element method, Equation (2.1.2) and (2.1.5) can be converted into matrix-vector forms as follows:

$$\mathbf{Su} = w(\sigma)\mathbf{f}, \quad (2.1.6)$$

$$\mathbf{Sg} = \mathbf{f}, \quad (2.1.7)$$

where $\mathbf{S}$ is the impedance matrix which depends on $c(\mathbf{x})$ and σ and $\mathbf{f}$ is a source vector whose components is $\delta(\mathbf{x}-\mathbf{s})$. By inverting the impedance matrix $\mathbf{S}$, we obtain the Laplace-domain wavefield $\mathbf{u}$ or Laplace-domain Green's function $\mathbf{g}$. In this paper, however, the detailed discretization process related to $\mathbf{S}$ is omitted because it is outside the scope of this study.

2.2 Logarithmic objective function for Laplace-domain waveform inversion (WI)

Laplace-domain WI proposed by Shin and Cha (2008) is an inversion algorithm that uses Laplace transformed data. This method is the same as waveform inversion using the zero frequency component of a damped wavefield. In the Laplace-domain WI algorithm, the amount of damping can be controlled by the Laplace constant σ.

To perform Laplace-domain WI, the objective function should be defined. To compensate for data amplitude loss due to exponential decay related to offset distance, a logarithmic objective function is generally adopted for the Laplace-domain WI algorithm. The logarithmic objective function of a single Laplace constant is expressed as

$$\mathrm{E}(\sigma) = \frac{1}{2}\sum_{s}\sum_{r}\left[\ln\left(\frac{d_{\mathbf{s},\mathbf{g}}(\sigma)}{u_{\mathbf{s},\mathbf{g}}(\sigma)}\right)\right]^2, \tag{2.2.1}$$

where $\mathbf{s}$ and $\mathbf{g}$ are the position vector of the sth source and the rth receiver, respectively. $u_{\mathbf{s},\mathbf{g}}$ and $d_{\mathbf{s},\mathbf{g}}$ are the modeled and observed wavefields of the sth source and the rth receiver, respectively, and σ is the Laplace constant. Expanding the logarithmic residual, $\ln\left(\frac{d_{\mathbf{s},\mathbf{g}}(\sigma)}{u_{\mathbf{s},\mathbf{g}}(\sigma)}\right)$, to the first-order term of a Taylor's series yields

$$\ln\left(\frac{d_{\mathbf{s},\mathbf{g}}(\sigma)}{u_{\mathbf{s},\mathbf{g}}(\sigma)}\right) \approx \sum_{j=1}^{M}\left\{\frac{\partial \ln\left(u_{\mathbf{s},\mathbf{g}}(\sigma)\right)}{\partial p_{\mathbf{m}_j}}\Delta p_{\mathbf{m}_j}\right\}, \tag{2.2.2}$$

where $\mathbf{m}_j$ is the position vector of jth model parameter, M is the number of model parameters, and $\Delta p_{\mathbf{m}_j}$ is the difference between the true model and the

estimated model of the jth parameter ($j = 1, \cdots, M$).

From Equation (2.2.2), we can recognize that the residual wavefield at a receiver $\ln\left(\frac{d_{\mathbf{s},\mathbf{g}}(\sigma)}{u_{\mathbf{s},\mathbf{g}}(\sigma)}\right)$ is generated by the superposition of scattered wavefields resulting from $\Delta p_{\mathbf{m}_j}$ (Woodward, 1992). Model differences at each point in the model $\Delta p_{\mathbf{m}_j}$ acts as a scatterer and $\Delta p_{\mathbf{m}_j}$ can be regarded as a weight of the following basis:

$$L(\mathbf{s}, \mathbf{g}, \mathbf{m}, \sigma) = \frac{\partial \ln\left(u_{\mathbf{s},\mathbf{g}}(\sigma)\right)}{\partial p_{\mathbf{m}_j}}, \tag{2.2.3}$$

where $L(\mathbf{s}, \mathbf{g}, \mathbf{x}, \sigma)$ is called the *wavepath* and represents a basis function constituting the residual wavefield, $\ln\left(\frac{d_{\mathbf{s},\mathbf{g}}(\sigma)}{u_{\mathbf{s},\mathbf{g}}(\sigma)}\right)$, as shown in Equation (2.2.2). In this case, the wavepath is obtained from the logarithmic objective function and is called the *Rytov wavepath*. To help clarify the Rytov wavepath, we provide a schematic diagram describing the relationship between the incident wavefield and scattering wavefield (Figure 1). The position vector of a source ($\mathbf{s}$), receiver ($\mathbf{g}$), model parameter ($\mathbf{m}$), and central point ($\mathbf{o}$) are within a specific window that is far from the source and receiver. $\mathbf{r}_{\boldsymbol{s}}$ represents the vector from $\mathbf{s}$ to $\mathbf{o}$ ($\mathbf{r}_{\boldsymbol{s}} = \mathbf{o} - \mathbf{s}$), $\mathbf{r}_{\boldsymbol{g}}$ represents the vector from $\mathbf{g}$ to $\mathbf{o}$ ($\mathbf{r}_{\boldsymbol{g}} = \mathbf{o} - \mathbf{g}$), and $\mathbf{x}$ represents the vector from $\mathbf{o}$ to $\mathbf{m}$ ($\mathbf{r}_{\boldsymbol{g}} = \mathbf{m} - \mathbf{o}$). Since the incident angle and scattering angle are always the same due to Snell's law, both angles can be equally represented by θ. $\hat{\mathbf{s}}$ and $\hat{\mathbf{g}}$ are direction vectors which are parallel to $\mathbf{r}_{\boldsymbol{s}}$ and $\mathbf{r}_{\boldsymbol{g}}$, respectively ($\hat{\mathbf{s}} = \frac{\mathbf{r}_s}{|\mathbf{r}_s|}$, $\hat{\mathbf{g}} = \frac{\mathbf{r}_g}{|\mathbf{r}_g|}$). $\mathbf{n}$ is a unit vector which is parallel to $\hat{\mathbf{s}} + \hat{\mathbf{g}}$ ($\mathbf{n} = \frac{\hat{\mathbf{s}}+\hat{\mathbf{g}}}{|\hat{\mathbf{s}}+\hat{\mathbf{g}}|}$).

The Rytov wavepath can be expressed using three Green's functions as follows:

$$L(\mathbf{s},\mathbf{g},\mathbf{m},\sigma)=\sigma^2\frac{g_0(\mathbf{m}|\mathbf{s},\sigma)g_0(\mathbf{m}|\mathbf{g},\sigma)}{g_0(\mathbf{g}|\mathbf{s},\sigma)}, \tag{2.2.4}$$

where $g_0(\mathbf{x}_2|\mathbf{x}_1,\sigma)$ is a Green's function of a single Laplace constant σ from $\mathbf{x}_1$ to $\mathbf{x}_2$ (Wu and Toksöz, 1987; Woodward, 1992). As shown in Equation (2.2.4), The Rytov wavepath is independent of the source wavelet because both the denominator and numerator have Laplace-domain wavefields such that the source wavelet components are canceled out. There can be some numerical instability caused by the inverse of $g_0(\mathbf{g}|\mathbf{s},\sigma)$ if $g_0(\mathbf{g}|\mathbf{s},\sigma)$ is too small. To stabilize the inverse process, it is recommended not to use data residuals observed from the receivers whose $g_0(\mathbf{g}|\mathbf{s},\sigma)$ is smaller than a certain threshold. Note that this paper assumes sloth (inverse of velocity squared) parameterization as follows:

$$p_{\mathbf{m}_j}=\frac{1}{c(\mathbf{m}_j)^2}. \tag{2.2.5}$$

If we assume velocity or slowness (inverse of velocity) parameterization rather than sloth parameterization, the function of the parameter is multiplied to Equation (2.2.4). However, the parameterization is outside the scope of this study. In this paper, for the sake of convenience, we proceed with the assumption of sloth parameterization

As shown in Equation (2.2.4), the Rytov wavepath in the Laplace domain can be expressed using the Laplace-domain Green's functions. To investigate the Rytov wavepath in Laplace domain more specifically and analyze the role of each Laplace constant by using the Rytov wavepath, we should determine the Green's function in the Laplace domain.

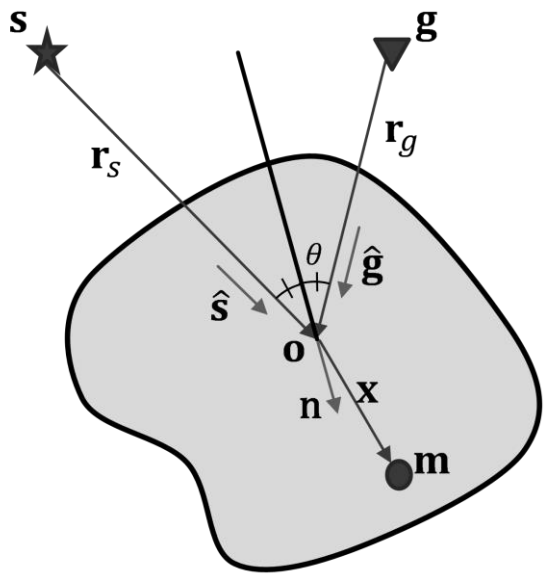

Figure 1 A schematic diagram describing the relationship between the incident wavefield and scattering wavefield. **s, g, m** and **o** are the position vectors of a source, receiver, model parameter and central point within a specific window that is far from the source and receiver, respectively. $\mathbf{r}_s$ represents the vector from **s** to **o** ($\mathbf{r}_s = \mathbf{o} - \mathbf{s}$), $\mathbf{r}_g$ represents the vector from **g** to **o** ($\mathbf{r}_g = \mathbf{o} - \mathbf{g}$), and **x** represents the vector from **o** to **m** ($\mathbf{r}_g = \mathbf{m} - \mathbf{o}$). Since the incident angle and scattering angle are always same due to Snell's law, both angles can be equally represented by θ. $\hat{\mathbf{s}}$ and $\hat{\mathbf{g}}$ are direction vectors which are parallel to $\mathbf{r}_s$ and $\mathbf{r}_g$, respectively ($\hat{\mathbf{s}} = \frac{\mathbf{r}_s}{|\mathbf{r}_s|}$, $\hat{\mathbf{g}} = \frac{\mathbf{r}_g}{|\mathbf{r}_g|}$). **n** is a unit vector which is parallel to $\hat{\mathbf{s}} + \hat{\mathbf{g}}$ ($\mathbf{n} = \frac{\hat{\mathbf{s}}+\hat{\mathbf{g}}}{|\hat{\mathbf{s}}+\hat{\mathbf{g}}|}$).

2.3 Laplace-domain Green's functions for a homogeneous acoustic unbounded medium

In this section, we briefly review the Laplace-domain Green's function for a homogeneous acoustic unbounded medium. The easiest way to obtain the Laplace-domain Green's function is by replacing angular frequency in the frequency-domain Green's functions with an imaginary component representing the Laplace constant. The 1D, 2D and 3D frequency-domain Green's functions can be expressed as follows (Ikelle and Amundsen, 2005):

$$\tilde{g}^{(3D)}(\mathbf{x}_1|\mathbf{x}_2,\omega) = \frac{\exp(ikR)}{4\pi R}, \tag{2.3.1}$$

$$\tilde{g}^{(2D)}(\mathbf{x}_1|\mathbf{x}_2,\omega) = \frac{i}{4}H_0^{(1)}(kR), \tag{2.3.2}$$

$$\tilde{g}^{(1D)}(\mathbf{x}_1|\mathbf{x}_2,\omega) = \frac{\exp(ikR)}{2ik}, \tag{2.3.3}$$

where

$$R = |\mathbf{x}_1 - \mathbf{x}_2| \tag{2.3.4}$$

and ω is angular frequency, $k\ (=\omega/c_0)$ is wavenumber. $H_0^{(1)}(x)$ is the zero order Hankel function of the first kind. If x is sufficiently large, $H_0^{(1)}(x)$ can be approximated asymptotically to $\sqrt{\frac{2}{\pi x}}\exp\left(i\left(x-\frac{\pi}{4}\right)\right)$. Therefore, if R is sufficiently large, the 2D Green's function $\tilde{g}^{(2D)}(\mathbf{x}_1|\mathbf{x}_2,\omega)$ in Equation (2.3.2) can be expressed as:

$$\tilde{g}^{(2D)}(\mathbf{x_1}|\mathbf{x_2},\omega)\sim\frac{i}{4}\sqrt{\frac{2}{\pi kR}}\exp\left(i\left(kR-\frac{\pi}{4}\right)\right). \tag{2.3.5}$$

If σ is the Laplace constant and ω is replaced by $i\sigma$ from Equations (2.3.1) – (2.3.5), we can obtain the 1D, 2D and 3D Laplace-domain Green's functions:

$$g^{(3D)}(\mathbf{x}_1|\mathbf{x}_2,\sigma)=\tilde{g}^{(3D)}(\mathbf{x}_1|\mathbf{x}_2,i\sigma)=\frac{\exp(-\alpha R)}{4\pi R}, \tag{2.3.6}$$

$$g^{(2D)}(\mathbf{x}_1|\mathbf{x}_2,\sigma)=\tilde{g}^{(2D)}(\mathbf{x}_1|\mathbf{x}_2,i\sigma)=\frac{i}{4}H_0^{(1)}(i\alpha R), \tag{2.3.7}$$

$$g^{(1D)}(\mathbf{x}_1|\mathbf{x}_2,\sigma)=\tilde{g}^{(1D)}(\mathbf{x}_1|\mathbf{x}_2,i\sigma)=\frac{\exp(-\alpha R)}{2\alpha}, \tag{2.3.8}$$

where $\alpha\ (=\sigma/c_0)$ is called the *attenuation constant*. Note that replacing ω with $i\sigma$ is equivalent to turning k into $i\alpha$. If $-\pi < \arg(x) \leq \pi/2$, the Hankel function whose domain is the set of purely imaginary numbers can be expressed with a modified Bessel function of the second kind as follows:

$$K_j(x)=\frac{\pi}{2}i^{j+1}H_j^{(1)}(ix). \tag{2.3.9}$$

Therefore, Equation (2.3.7) can be expressed as:

$$g^{(2D)}(\mathbf{x}_1|\mathbf{x}_2,\sigma)=\frac{1}{2\pi}K_0(\alpha R). \tag{2.3.10}$$

If R is sufficiently large, Equation (2.3.10) can be approximated as:

$$g^{(2D)}(\mathbf{x}_1|\mathbf{x}_2,\sigma)\sim\frac{\exp(-\alpha R)}{\sqrt{8\pi\alpha R}}. \tag{2.3.11}$$

Generally, the Laplace-domain Green's function can be expressed asymptotically as:

$$g^{(nD)}(\mathbf{x}_1|\mathbf{x}_2,\sigma)\sim\frac{\exp(-\alpha R)}{A_n(R,\alpha)}, \tag{2.3.12}$$

where

$$A_n(R,\alpha)=\begin{cases}4\pi R & if\ n=3\\ \sqrt{8\pi\alpha R} & if\ n=2.\\ 2\alpha & if\ n=1\end{cases} \tag{2.3.13}$$

Using these Green's functions, we express the Rytov wavepath in the Laplace domain in the next section.

2.4 Rytov wavepath in the Laplace domain

The Source Green's function and Receiver Green's function can be expressed as follows:

$$g^{(nD)}(\mathbf{m}|\mathbf{s},\sigma)\sim\frac{\exp(-\alpha R_{\mathbf{ms}})}{A_n(R_{\mathbf{ms}},\alpha)}, \tag{2.4.1}$$

$$g^{(nD)}(\mathbf{m}|\mathbf{g},\sigma)\sim\frac{\exp\left(-\alpha R_{\mathbf{mg}}\right)}{A_n(R_{\mathbf{mg}},\alpha)}, \tag{2.4.2}$$

$$g^{(nD)}(\mathbf{g}|\mathbf{s},\sigma)\sim\frac{\exp\left(-\alpha R_{\mathbf{gs}}\right)}{A_n(R_{\mathbf{gs}},\alpha)}, \tag{2.4.3}$$

where

$$\begin{aligned} R_{\mathbf{ms}} &= |\mathbf{m}-\mathbf{s}| = |\mathbf{x}+\mathbf{r_s}|, \\ R_{\mathbf{mg}} &= |\mathbf{m}-\mathbf{g}| = \left|\mathbf{x}+\mathbf{r_g}\right|, \\ R_{\mathbf{gs}} &= |\mathbf{g}-\mathbf{s}| = \left|\mathbf{r_s}-\mathbf{r_g}\right|. \end{aligned} \tag{2.4.4}$$

Note that the symbols are illustrated in Figure 1. If the source and receiver are far from the object, we can use the Fraunhofer approximation for the Green's functions (Wu and Toksöz, 1987) as follows:

$$g^{(nD)}(\mathbf{m}|\mathbf{s},\sigma)\approx\frac{\exp\left(-\alpha(|\mathbf{r_s}|+\hat{\mathbf{s}}\cdot\mathbf{x})\right)}{A_n(|\mathbf{r_s}|+\hat{\mathbf{s}}\cdot\mathbf{x},\alpha)}, \tag{2.4.5}$$

$$g^{(nD)}(\mathbf{m}|\mathbf{g},\sigma)\approx\frac{\exp\left(-\alpha\left(\left|\mathbf{r_g}\right|+\hat{\mathbf{g}}\cdot\mathbf{x}\right)\right)}{A_n\left(\left|\mathbf{r_g}\right|+\hat{\mathbf{g}}\cdot\mathbf{x},\alpha\right)}. \tag{2.4.6}$$

By putting the analytic Green's functions (Equation (2.4.5) and (2.4.6)) into Equation (2.2.4), we can obtain the Rytov wavepath expressed by a decaying function:

$$L(\mathbf{s},\mathbf{g},\mathbf{m},\sigma)$$

$$\approx \sigma^2 \frac{\exp\left(-\alpha\left(|\mathbf{r}_s|+|\mathbf{r}_\mathbf{g}|\right)\right)\exp(-\alpha(\hat{\mathbf{s}}+\hat{\mathbf{g}})\cdot\mathbf{x})}{g_0(\mathbf{g}|\mathbf{s},\sigma)A_n(|\mathbf{r}_\mathbf{s}|+\hat{\mathbf{s}}\cdot\mathbf{x},\alpha)A_n\left(|\mathbf{r}_\mathbf{g}|+\hat{\mathbf{g}}\cdot\mathbf{x},\alpha\right)}. \quad (2.4.7)$$

From Equation (2.4.7), it can be seen that the Rytov wavepath is decayed by both the exponential term $\exp(-\alpha(\hat{\mathbf{s}}+\hat{\mathbf{g}})\cdot\mathbf{x})$ and the geometrical spreading effect $1/[A_n(|\mathbf{r}_\mathbf{s}|+\hat{\mathbf{s}}\cdot\mathbf{x},\alpha)A_n\left(|\mathbf{r}_\mathbf{g}|+\hat{\mathbf{g}}\cdot\mathbf{x},\alpha\right)]$. The value of $1/[A_n(|\mathbf{r}_\mathbf{s}|+\hat{\mathbf{s}}\cdot\mathbf{x},\alpha)A_n\left(|\mathbf{r}_\mathbf{g}|+\hat{\mathbf{g}}\cdot\mathbf{x},\alpha\right)]$ in 1D, 2D and 3D is proportional to 1, $1/\sqrt{(|\mathbf{r}_\mathbf{s}|+\hat{\mathbf{s}}\cdot\mathbf{x})\left(|\mathbf{r}_\mathbf{g}|+\hat{\mathbf{g}}\cdot\mathbf{x}\right)}$ and $1/[(|\mathbf{r}_\mathbf{s}|+\hat{\mathbf{s}}\cdot\mathbf{x})\left(|\mathbf{r}_\mathbf{g}|+\hat{\mathbf{g}}\cdot\mathbf{x}\right)]$, respectively.

Sirgue and Pratt (2004) assumes a far-field to obtain a frequency domain wavepath. We similarly assume a far-field in this process to obtain a wavepath in the Laplace domain ($|\mathbf{x}| \ll |\mathbf{r}_\mathbf{s}|$ and $|\mathbf{x}| \ll |\mathbf{r}_\mathbf{g}|$). If we assume that α is moderately large and a far-field approximation, the degree of attenuation by the inverse function $1/A_n(|\mathbf{r}_\mathbf{g}|+\hat{\mathbf{g}}\cdot\mathbf{x},\alpha)$ with respect to $\mathbf{x}$ is negligible compared to the degree of attenuation by the exponential function $\exp\left(-\alpha\left(|\mathbf{r}_\mathbf{g}|+\hat{\mathbf{g}}\cdot\mathbf{x}\right)\right)$ with respect to $\mathbf{x}$. Then $A_n(|\mathbf{r}_\mathbf{g}|+\hat{\mathbf{g}}\cdot\mathbf{x},\alpha)$ can be approximately regarded as the function independent of $\mathbf{x}$. Thus, we can assume that the effect of geometrical spreading is negligible. Equation (2.4.5) and (2.4.6) can now be approximated as follows:

$$g^{(nD)}(\mathbf{m}|\mathbf{s},\sigma) \approx \frac{\exp\left(-\alpha(|\mathbf{r}_\mathbf{s}|+\hat{\mathbf{s}}\cdot\mathbf{x})\right)}{A_n(|\mathbf{r}_\mathbf{s}|,\alpha)}, \quad (2.4.8)$$

$$g^{(nD)}(\mathbf{m}|\mathbf{g},\sigma) \approx \frac{\exp\left(-\alpha\left(|\mathbf{r}_\mathbf{g}|+\hat{\mathbf{g}}\cdot\mathbf{x}\right)\right)}{A_n\left(|\mathbf{r}_\mathbf{g}|,\alpha\right)}. \quad (2.4.9)$$

By putting the analytic Green's functions (Equation (2.4.8) and (2.4.9)) into Equation (2.2.4), we can obtain the Rytov wavepath expressed by an exponentially decaying function varying with attenuation constant:

$$L^{(nD)}(\mathbf{s},\mathbf{g},\mathbf{m},\sigma) \approx B^{(nD)}(\mathbf{s},\mathbf{g},\mathbf{o},\sigma)\exp(-\boldsymbol{\alpha}(\mathbf{s},\mathbf{g},\mathbf{o},\sigma)\cdot\mathbf{x}), \quad (2.4.10)$$

where

$$\boldsymbol{\alpha}(\mathbf{s},\mathbf{g},\mathbf{o},\sigma) = \frac{2\sigma}{c_0} cos\theta\,\mathbf{n}, \quad (2.4.11)$$

and

$$B^{(nD)}(\mathbf{s},\mathbf{g},\mathbf{o},\sigma) = \begin{cases} \dfrac{\sigma^2 \exp\left(-\alpha\left(|\mathbf{r_s}| + |\mathbf{r_g}|\right)\right)}{g_0^{(3D)}(\mathbf{g}|\mathbf{s},\sigma)} \dfrac{1}{16\pi^2|\mathbf{r_s}||\mathbf{r_g}|} & if\ n = 3 \\ \dfrac{\sigma^2 \exp\left(-\alpha\left(|\mathbf{r_s}| + |\mathbf{r_g}|\right)\right)}{g_0^{(2D)}(\mathbf{g}|\mathbf{s},\sigma)} \dfrac{1}{8\pi\alpha\sqrt{|\mathbf{r_s}||\mathbf{r_g}|}} & if\ n = 2 \\ \dfrac{\sigma^2 \exp\left(-\alpha\left(|\mathbf{r_s}| + |\mathbf{r_g}|\right)\right)}{g_0^{(1D)}(\mathbf{g}|\mathbf{s},\sigma)} \dfrac{1}{4\alpha^2} & if\ n = 1 \end{cases}. \quad (2.4.12)$$

For simplicity, we introduce the notation $\boldsymbol{\alpha}(\mathbf{s},\mathbf{g},\mathbf{o},\sigma)$ and we will call it the *scattering attenuation constant vector*. $\boldsymbol{\alpha}(\mathbf{s},\mathbf{g},\mathbf{o},\sigma)$ defines the steepness of the Rytov wavepath decaying exponentially in the direction of the $\mathbf{n}$ vector near the scattering point $\mathbf{o}$. $B^{(nD)}(\mathbf{s},\mathbf{g},\mathbf{o},\sigma)$ represents the amplitude of the Rytov wavepath. Note that $\boldsymbol{\alpha}(\mathbf{s},\mathbf{g},\mathbf{o},\sigma)$ is independent of $\mathbf{x}$ and $B^{(nD)}(\mathbf{s},\mathbf{g},\mathbf{o},\sigma)$ is also independent of $\mathbf{x}$ as long as $|\mathbf{x}| \ll |\mathbf{r_s}|$ and $|\mathbf{x}| \ll |\mathbf{r_g}|$. Thus, they can be regarded as constants near the scattering point $\mathbf{o}$. Hence, it can be confirmed that the Rytov wavepath in the Laplace domain is approximately an exponential decaying real basis function, whose scattering attenuation constant vector is $\boldsymbol{\alpha}(\mathbf{s},\mathbf{g},\mathbf{o},\sigma)$ in the space domain. This is shown in Equation (2.4.10).

What is important in Equation (2.4.11) is that the amplitude of the scattering attenuation constant vector is affected simultaneously by the Laplace constant σ and incident angle θ. Therefore, even if a single Laplace constant is used, the amplitude of the scattering attenuation constant varies depending on the incident angle range. The relationship among the scattering attenuation constant, Laplace constant and the incident angle in the Laplace domain corresponds exactly to the relationship among the scattering wavenumber, frequency and incident angle in the frequency domain. This similarity provides an opportunity to apply the analysis used in the frequency domain similarly to the Laplace domain.

In the following sections, we perform various analyses using the fact that the Laplace-domain wavepath consists of real exponentially decaying bases dependent on the scattering attenuation constant vector. And the fact that the scattering attenuation constant vector is dependent on both the Laplace constant and the incident angle.

2.5 Vertical components of wavepath in the Laplace domain considering the geometrical spreading effect

The Rytov wavepath in the Laplace domain is affected by the geometric spreading effect as well as the attenuation constant. Of course, the attenuation due to this geometrical spreading effect is much smaller than the attenuation due to the exponential term as shown in (2.4.7). However, since the attenuation due to the geometrical spreading effect is not well distinguished from the attenuation due to the exponential term in the Laplace-domain WI algorithm, the geometrical spreading effect acts like an additional exponential term. In this section, we explain how geometrical spreading affects the wavepath in the Laplace domain.

According to Appendix A, the geometrical spreading effect can be considered for the vertical wavepath as follows:

$$L^{(nD)}(\mathbf{s},\mathbf{g},\mathbf{m},\sigma) \approx B^{(nD)}(\mathbf{s},\mathbf{g},\mathbf{o},\sigma)\exp\left(-\frac{2\sigma_{app}^{(nD)}}{c_0}cos\theta z\right), \quad (2.5.1)$$

where

$$\sigma_{app}^{(nD)} = \begin{cases} \sigma + \dfrac{c_0}{R} & if\ n = 3 \\ \sigma + \dfrac{c_0}{2R} & if\ n = 2 \\ \sigma & if\ n = 1 \end{cases}. \quad (2.5.2)$$

where $\sigma_{app}^{(nD)}$ is the *n-dimensional apparent Laplace constant*. As shown in Equation (2.5.2), the geometrical spreading effect causes the additional attenuation increasing the apparent Laplace constants. Also, we can confirm that this influence of geometrical spreading decreases as R increases or σ increases (far-field approximation). Therefore, this additional attenuation

caused by the geometrical spreading effect can be neglected when σ or R is large enough.

2.6 Numerical examples

We examine whether the attenuation constant in the far-field condition follows Equation (2.4.11). To confirm this, we check whether the attenuation constants of the wavepath remain unchanged for varying offsets and Laplace constants that keep the value of the right-hand side of Equation (2.4.11) the same.

Figure 2 (a), (b) and (c) show the 3D wavepath in the Laplace domain at Laplace constants 7.17, 10.0, and 14.9 s^{-1}, with offsets of 0.35, 2.0, and 3.7 km respectively. These offsets keep the right-hand side of Equation (2.4.11) equal at 1km target-depth in the middle of the model. As shown in the vertical profile of these wavepaths, we can see that the amplitudes are attenuated with similar ratios for the same height difference at 1km depth.

For a more detailed comparison, Figure 3 compares the exponential function using the expected scattering attenuation constant and the vertical profiles of wavepaths normalized by $B^{(3D)}(\mathbf{s}, \mathbf{g}, \mathbf{o}, \sigma)$ shown in Equation (2.4.12) with the logarithmic scale. If the normalized vertical profiles in the logarithmic scale are arranged tangentially, the attenuation constants are the same. Figure 3 shows that the normalized profiles of (b) and (c) are almost tangent to the exponential function using the expected scattering attenuation constant at 1 km in depth. The normalized profile of (a), however, is not exactly tangent to the exponential function. In this case, the geometrical spreading effect cannot be ignored because the distance from the source or receiver to target is not far enough.

Figure 4 shows the vertical profiles of wavepaths obtained from the Laplace constants satisfying the Equation (2.5.2) considering the geometrical spreading effect for the offsets used in Figure 3. As shown in Figure 4, all the normalized

profiles are tangent to the exponential function using the expected scattering attenuation constant at 1 km in depth. This shows that Equation (2.5.2) holds for the general case, and should be used if the far-field assumption is not established.

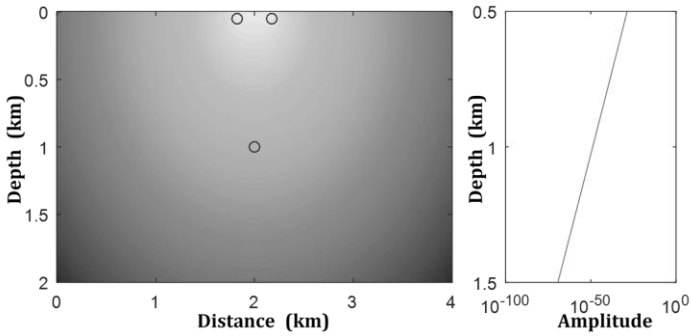

(a)

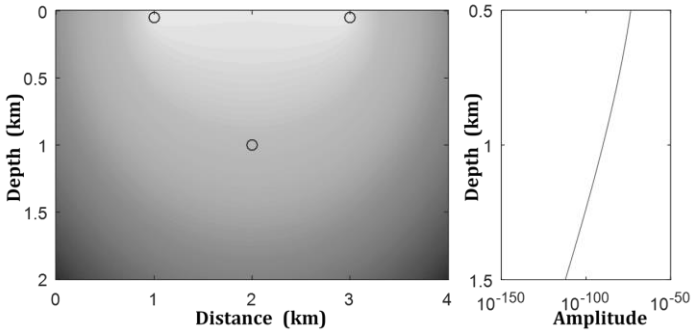

(b)

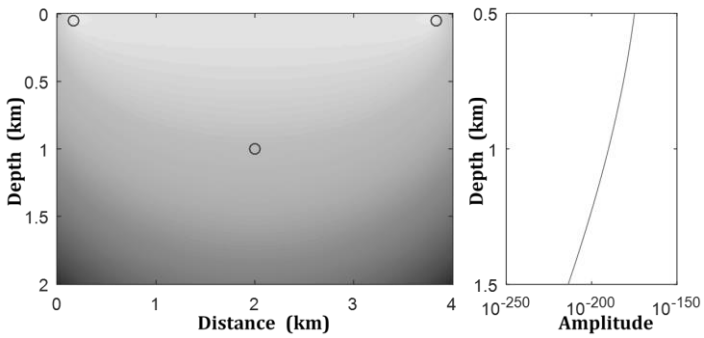

(c)

Figure 2 The Laplace-domain Rytov wavepath where the geometrical spreading effect is not compensated and its vertical amplitude profile is near the target point. The upper two circles of each figure represent source and receiver location. The lower circle of each figure represents the target point (x: 2km, z: 1km). Each wavepath uses 0.35km offset and 7.17 s^{-1} Laplace constant for (a), 2km offset and 10.0 s^{-1} Laplace constant for (b), 3.7km offset and 14.9 s^{-1} Laplace constant for (c).

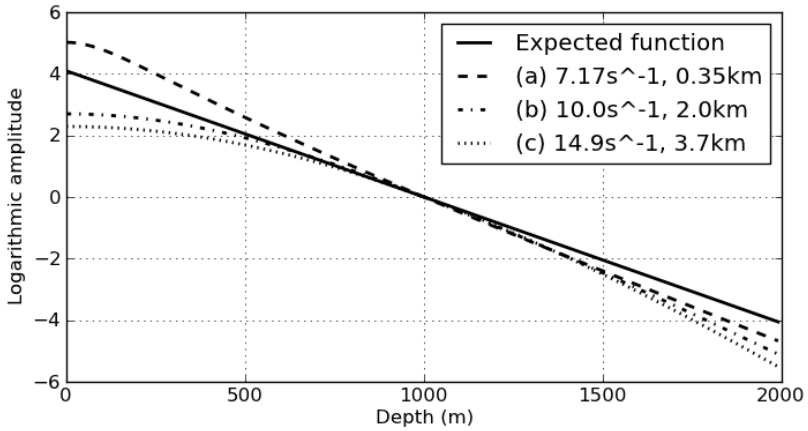

Figure 3 Vertical profiles of the normalized relative amplitudes of wavepaths where the geometrical spreading effect is not compensated.

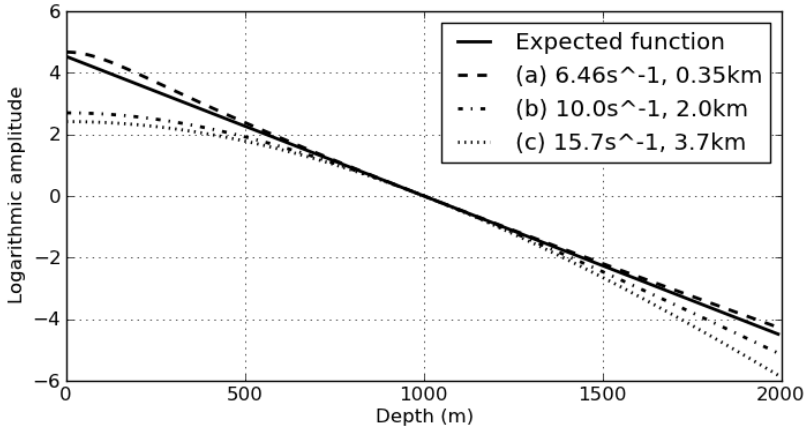

Figure 4 Vertical profiles of the normalized relative amplitudes of wavepaths where the geometrical spreading effect is compensated.

Chapter 3 Truncated Gauss-Newton method for Laplace-domain WI

The Gauss-Newton method, which considers the Hessian matrix, can be a solution in the ill-conditioned problem (Press et al., 1992; Strutz, 2016). Pratt et al. (1998) verified that application of the Gauss-Newton method, to frequency-domain WI greatly improves the convergence rate. In this chapter, we show that the Gauss-Newton method exerts greater efficacy in Laplace-domain WI due to its ill-conditioning. We also suggest how to efficiently apply the truncated Gauss-Newton method, which adopts the conjugate gradient (CG) method, to Laplace-domain WI. The numerical example using the BP benchmark model also confirms that the truncated Gauss-Newton method is superior to the gradient descent method.

3.1 Gauss-Newton method and ill-conditioned problems

Before describing why Laplace-domain WI requires the Gauss-Newton method, we explain what ill-conditioned problems are and why the gradient descent method is not proper for an ill-conditioned problem.

An ill-conditioned problem refers to a problem where a small input adjustment causes a large variation in the output. When applying this to the inverse problem, a small change in observed data results in a large change in the estimation of the model parameters. The measurement of ill-conditioning is typically represented by a condition number $\kappa(L)$, which is expressed as a supremum in the ratio of change in data to change in model parameter (Trefethen and Bau, 1997):

$$\kappa(L) = \sup_{\delta d} \left(\frac{\|\delta m\|}{\|m\|} \right) / \left(\frac{\|\delta d\|}{\|d\|} \right). \tag{3.1.1}$$

$\kappa(L)$ also can be defined as the square root of the condition number of the Hessian, H $(= L^T L)$:

$$\kappa(L) = \sqrt{\kappa(H)}. \tag{3.1.2}$$

$\kappa(H)$ can be defined as the ratio of the maximum eigenvalue of the Hessian, λ_{max}, to the minimum eigenvalue of the Hessian, λ_{min}:

$$\kappa(H) = \frac{|\lambda_{max}|}{|\lambda_{min}|}. \tag{3.1.3}$$

Therefore, $\kappa(L)$ can be expressed as:

$$\kappa(L) = \frac{\sqrt{\lambda_{max}}}{\sqrt{\lambda_{min}}}. \tag{3.1.4}$$

Here, each eigenvalue of the Hessian represents the sensitivity of the data in

the direction of the eigenvector of each model parameter. Thus, the fact that an eigenvalue is small means that the data hardly changes with respect to the corresponding eigenvector of the model parameter. That is, the condition number is the ratio of the minimum value and the maximum value of the sensitivity of the data in the direction of the eigenvectors of model parameters. If λ_{max} is close to λ_{min}, then $\kappa(L) \cong 1$. We call the problem which has a small condition number like this a *well-conditioned problem*. If λ_{max} is much larger than λ_{min}, then $\kappa(L) \gg 1$. We call the problem which has a large condition number like this an *ill-conditioned problem*.

The problems that arise with the gradient descent method as $\kappa(L)$ increases can be understood more easily by investigating Figure 5. Figure 5 shows the contour of the objective function changing with respect to two model parameters:

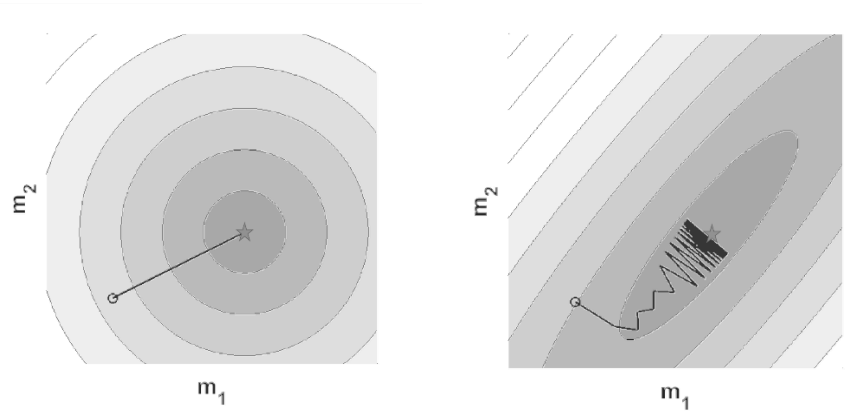

(a) (b)

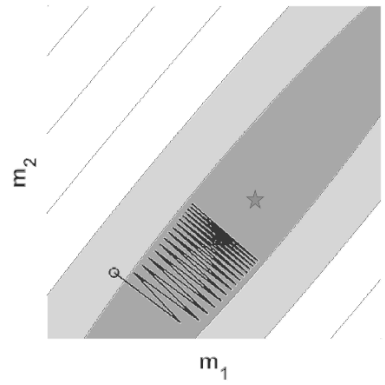

(c)

Figure 5 Contour plots of the objective functions depending on the condition number. (a), (b) and (c) show the variation of the objective functions for the parameters when $\kappa(L)$ = 1.00, 4.00, and 6.67, respectively. The larger the condition number, the larger the anisotropy of the ellipse. Moreover, as the condition number increases, the update directions of the gradient descent method zigzags and the convergence speed decreases. The asterisks represent the global minima.

The largest and shortest diameters of each ellipsoidal contour of the objective function in Figure 5 are closely related to λ_{max} and λ_{min}. The ratio between largest and shortest diameters is same as the ratio between λ_{max} and λ_{min}. Therefore, as $\kappa(L)$ increases, the contours become more anisotropic.

The anisotropy, that becomes stronger as $\kappa(L)$ increases, greatly affects the convergence rate of the gradient descent method (Press et al., 1992; Strutz, 2016). This is because the larger the difference between the long axis and the short axis of the contour, the more updates of the gradient descent method show zigzag shapes as illustrated in Figure 5. This zigzag-shaped update occurs more frequently when the gradient direction vector is nearly orthogonal to the shortest direction to the local minimum. These zigzag-shaped updates of the gradient descent method result in many iterations needed to reach a local minimum with sufficient accuracy.

The Gauss-Newton method, which considers the Hessian matrix, can be an alternative approach to the ill-conditioned problem (Press et al., 1992; Strutz, 2016). In contrast to the gradient descent method, if the problem is perfectly linear, the Gauss-Newton method converges to the global minimum with a single iteration. Generally, the Gauss-Newton method converges in fewer iterations, without zigzag shapes, even though the problem is nonlinear and ill-conditioned. Therefore, in the case of a large condition number, it is necessary to use the Gauss-Newton method, considering the Hessian, rather than gradient descent method for fast convergence.

3.2 Ill-conditioning of the Laplace-domain WI algorithm

Before explaining the ill-conditioning of the problem of waveform inversion in the Laplace domain, we first describe the well-conditioning of frequency-domain WI. According to Sirgue and Pratt (2004), the Born wavepath of the frequency domain, $L_f(\mathbf{x}, \mathbf{k})$, can be approximately expressed as:

$$L_f(\mathbf{x}, \mathbf{k}) \approx A(\mathbf{k}) \exp(-i\mathbf{k} \cdot \mathbf{x}). \tag{3.2.1}$$

where $\mathbf{k}$ is a scattering wavenumber vector and $A(\mathbf{k})$ is a spectrum of $\mathbf{k}$. If $\mathbf{x}$ is discretized for a simple explanation, we convert $L_f(\mathbf{x}, \mathbf{k})$ as follows:

$$L_f(i, \mathbf{k}) \approx A(\mathbf{k}) \exp(-i\mathbf{k} \cdot \mathbf{x}_i). \tag{3.2.2}$$

In order for frequency-domain WI to be well-solved with the gradient descent method, the condition number of L_f, $\kappa(L_f)$, should be close to 1 as described in Chapter 3.1. To understand $\kappa(L_f)$, the condition number of the Hessian, H_f $(= L_f^T L_f^*)$, must first be grasped. By using Equation (3.2.2), we can express the (i, j) component of the Hessian matrix, $H_f(i, j)$, as follows:

$$\begin{aligned} H_f(i,j) &= \left(L_f^T L_f^*\right)_{i,j} \\ &= Re\left[\int A(\mathbf{k})^2 \exp\left(-i\mathbf{k} \cdot \left(\mathbf{x}_i - \mathbf{x}_j\right)\right) d\mathbf{k}\right]. \end{aligned} \tag{3.2.3}$$

The matrix H_f can be classified as a symmetric Toeplitz matrix. In the ideal case of a full bandwidth and a normalized spectrum ($A(\mathbf{k}) = 1$), the Hessian H_f in the frequency domain becomes the unitary matrix:

$$H_f(i, j) = \delta_{ij}. \tag{3.2.4}$$

As the matrix approaches to the unit matrix, the condition number of the matrix decreases. Therefore, in the case of frequency-domain WI, the condition

number of the Hessian, $\kappa(H_f)$, decreases when the bandwidth of scattering wavenumbers increases. Therefore, frequency-domain WI can be a well-conditioned problem as long as a wide frequency band is guaranteed.

As expressed in Chapter 2.4, the Rytov wavepath in the Laplace domain is approximately an exponential decaying real basis function whose scattering attenuation constant vector is $\boldsymbol{\alpha}(\mathbf{s}, \mathbf{g}, \mathbf{o}, \sigma)$ in the space domain as shown in Equations (2.4.10) and (2.4.11). If all amplitude variations are canceled by appropriate scaling schemes and $|\mathbf{x}|$ is not large relative to the total length of ray (far-field approximation), then the wavepath in the Laplace domain can be approximated by an exponential basis as:

$$L_l(\mathbf{x}, \boldsymbol{\alpha}) \approx B(\boldsymbol{\alpha}) \exp(-\boldsymbol{\alpha} \cdot \mathbf{x}). \tag{3.2.5}$$

where $\boldsymbol{\alpha}$ is a scattering attenuation constant vector and $B(\boldsymbol{\alpha})$ is a spectrum of $\boldsymbol{\alpha}$. If $\mathbf{x}$ is discretized for a simple explanation, we convert $L_l(\mathbf{x}, \boldsymbol{\alpha})$ to:

$$L_l(i, \boldsymbol{\alpha}) \approx B(\boldsymbol{\alpha}) \exp(-\boldsymbol{\alpha} \cdot \mathbf{x}_i). \tag{3.2.6}$$

The Hessian matrix of the Laplace domain, H_l, can then be expressed as:

$$H_l(i,j) = \left(L_l^T L_l\right)_{i,j} = \int \; B(\boldsymbol{\alpha})^2 \exp\left(-\boldsymbol{\alpha} \cdot \left(\mathbf{x_i} + \mathbf{x_j}\right)\right) d\boldsymbol{\alpha}. \tag{3.2.7}$$

The matrix H_l is classified as a real positive semidefinite Hankel matrix, as shown in the following equation (Beckermann, 2000):

$$H_l(i,j) = \left(h_{i+j}\right)_{i,j=0,1,\cdots,M}, \qquad h_k = \int x^k d\mu(x). \tag{3.2.8}$$

This real positive semidefinite Hankel matrix is known to have an extremely large condition number. According to Beckermann (2000) the condition number of the real positive semidefinite Hankel matrix increases exponentially with respect to the dimension of H_l, which implies the number of model parameters. The Hilbert matrix, a special case of the real positive semidefinite

Hankel matrix, is the most famous example of a large condition number. The Hilbert matrix is represented by the Hessian of the Laplace domain H_l when the integral range of Equation (3.2.7) is from 0 to ∞ and $B(\boldsymbol{\alpha}) = 1$. It can be expressed as:

$$H_l(i,j) = \frac{1}{i+j-1}. \tag{3.2.9}$$

The condition number of the Hilbert matrix $\kappa(H_f)$ grows like $(1+\sqrt{2})^{4M}/\sqrt{M}$ (Todd, 1954; Wilkinson, 1965). This implies that the condition number of the wavepath of the Laplace domain $\kappa(L_f)$ grows like $(1+\sqrt{2})^{2M}/\sqrt[4]{M}$. Note that this extremely high condition number is the result of full positive attenuation constants. The large condition number of the full-bandwidth wavepath of Laplace-domain WI contrasts greatly with the small condition number of the full-bandwidth wavepath of the frequency-domain WI.

This shows that Laplace-domain WI is always an ill-conditioned problem with or without the wide bandwidth of the attenuation constant. In the Laplace-domain WI algorithm, the gradient descent method converges too slowly due to this ill-conditioning of the Laplace-domain wavepath. Therefore, Laplace-domain WI cannot guarantee a reasonable convergence rate without a method considering the Hessian matrix, such as the Gauss-Newton method.

3.3 Truncated Gauss-Newton method

An effective solution for suppressing the crosstalk effect is the adoption of the Gauss-Newton method. In the Gauss-Newton method, a Hessian matrix is generated and solved to scale the parameter updates. The Hessian matrix consists of the correlation terms between the partial derivatives of the Laplace wavefields with respect to two parameters. The (i,j) components of the Hessian matrix can be expressed:

$$H_{ij} = \sum_{k}^{N_s N_r} \frac{\partial \log(u_k)}{\partial p_i} \frac{\partial \log(u_k)}{\partial p_j} = C(p_i, p_j). \tag{3.3.1}$$

As shown in the definition, the Hessian matrix has cross-correlation terms between two different parameters on the off-diagonal position, which is the main cause of the inaccuracy of model updates. This inaccuracy of model updates, caused by large off-diagonal components, results in a slow convergence rate. We call this inaccuracy caused by the off-diagonal components of the Hessian *crosstalk effect*. Consideration of these off-diagonal terms plays a role in suppressing the crosstalk effect caused by the cross-correlation terms (Pratt et al., 1998). Therefore, we can obtain more accurate updates of parameters without the crosstalk effect by generating and solving the Hessian matrix.

However, the Gauss-Newton method is hard to apply to WI because of its high computational cost. This is related to explicitly calculating and saving the Hessian matrix, which is an extremely huge matrix. To improve the computational efficiency, the truncated Gauss-Newton method which adopts the conjugate gradient (CG) method is widely used to consider the Hessian matrix (Golub and Van Loan, 1996; Hu et al., 2009; Pyun et al., 2011, Métivier

et al., 2013). In the truncated Gauss-Newton method, the Hessian-vector product allows the Gauss-Newton method to be implemented without explicitly calculating or saving the Hessian matrix. Therefore, the computational efficiency of the Gauss-Newton method is improved by using the truncated Gauss-Newton method. In a paper by Pyun et al. (2011), the truncated Gauss-Newton method algorithm was applied to the logarithmic misfit function in the frequency domain. We followed the method of Pyun et al. (2011) but applied it to Laplace-domain WI instead of frequency-domain WI. Further details of the truncated Gauss-Newton method is explained in Appendix B. Note that any optimization scheme that considers the off-diagonal components of the Hessian matrix, such as the quasi-Newton l-BFGS method (Wright and Nocedal, 1999), can be used to suppress the distortion effect of the WI in the Laplace domain.

Note that the convergence rate of the truncated Gauss-Newton method is also affected by the condition number of the Hessian matrix. The number of iterations of CG in the truncated Gauss-Newton method algorithm is proportional to $\kappa(L_l)\left(=\sqrt{\kappa(H_l)}\right)$. Therefore, the convergence rate of CG slows down as the condition number of the Hessian increases. Nevertheless, according to Shewchuk (1994), the truncated Gauss-Newton method converges $\sqrt{\kappa(H_l)}$ times faster than the gradient descent method in a locally linear case. That is, the convergence rate of the gradient descent method is more sensitive to $\kappa(H_l)$ than that of the truncated Gauss-Newton method. This implies that the truncated Gauss-Newton method is a better choice for fast convergence than the gradient descent method when solving ill-conditioned problems such as Laplace-domain WI.

3.4 Stopping criterion

While solving the Hessian matrix completely provides a correct answer in linear inverse problems, the nonlinear inverse problem is problematic if the Hessian is solved too completely. This phenomenon is called *over-solving*. This over-solving problem can be solved by constraining the degree to which the Hessian is solved depending on how much the objective function is locally quadratic. Given that for Laplace-domain WI we solve a nonlinear inverse problem, the problem of over-solving should be suppressed as much as possible.

To prevent over-solving in the CG method, a stopping criterion for the CG method suggested by Eisenstat et al. (1994) and Métivier et al. (2013) can be used. According to Eisenstat et al. (1994) and Métivier et al. (2013), the CG iterations should stop whenever

$$\|H(p_k)\Delta p_k + g(p_k)\| \leq \eta_k \|\nabla E(p_k)\|, \tag{3.4.1}$$

where p_k is the vector of the parameters, $H(p_k)$ is the Hessian matrix, and $g(p_k)$ is the gradient direction vector of kth outer iteration . The value η_k is called the forcing term. According to Métivier et al. (2013), the following definition of the forcing term η_k, proposed by Eisenstat et al. (1994), provides a good convergence speed in the Gauss-Newton algorithm:

$$\eta_k = \frac{\|g(p_k)\| - \|g(p_{k-1}) + H(p_{k-1})\Delta p_{k-1}\|}{\|g(p_{k-1})\|}. \tag{3.4.2}$$

To prevent the forcing term from being too restrictive, the following safeguards should be implemented:

$$\text{If } \eta_{k-1}^{(1+\sqrt{5})/2} > 0.1, \text{then } \eta_k = \max\left\{\eta_k, \eta_{k-1}^{(1+\sqrt{5})/2}\right\} \tag{3.4.3}$$

and

$$\text{If } \eta_k > 1, \text{then } \eta_k = 0.9. \tag{3.4.4}$$

In this paper, we applied this forcing term to the stopping criterion for the truncated Gauss-Newton method in the Laplace domain.

3.5 Numerical examples

In this section, we demonstrate how the inversion result of synthetic seismic data can be improved using the truncated Gauss-Newton method instead of the gradient descent method. Laplace-domain WI is a technique that is specialized in estimating velocity models with salt domes. However, the conventional Laplace-domain WI cannot provide a high resolution model for low velocity layer under salt domes within a reasonable time. By contrast, the truncated Gauss-Newton method is expected to show faster convergence in these areas. Therefore, we used the BP benchmark model (Figure 6(a)), which includes three distinct salt domes, to test whether the low velocity layer under the salt domes can be constructed accurately.

The BP benchmark model is used to generate time-domain seismograms. The seismic data was generated using a 6th order finite-difference method (FDM). The marine seismic experiment was conducted for this test. There are 418 sources and 301 receivers on a streamer. The maximum offset is 15 km. The depth of sources and receivers is 50m and their interval is 50m. Figure 6(b) shows the initial model for the Laplace-domain WI test. We constrained the maximum velocity to 4800 m/s and the minimum velocity to 1486 m/s.

To verify the effectiveness of the truncated Gauss-Newton method in Laplace-domain WI, we inverted the BP benchmark model (Figure 6(a)) with and without considering the off-diagonal components of the Hessian matrix. We then compared the updates of the parameter and velocity models. To implement this test, we used two methods for the BP benchmark model: the truncated Gauss-Newton method and the gradient descent method scaled by the diagonal components of the Hessian matrix. By comparing the updates of the parameters and the inverted velocity models, we can verify the effectiveness of considering

the off-diagonal components of the Hessian matrix.

In the numerical test of the truncated Gauss-Newton method, the forcing term η_k in Equation (3.4.2) was used, and the additional safeguards in Equation (3.4.3) and Equation (3.4.4) were implemented. To prevent the CG iteration from being too large, we set the maximum number of the CG iteration to 30 as an additional safeguard. Because the forcing term of the first iteration η_1 cannot be defined by Equation (3.4.2), we set η_1 to 0.05.

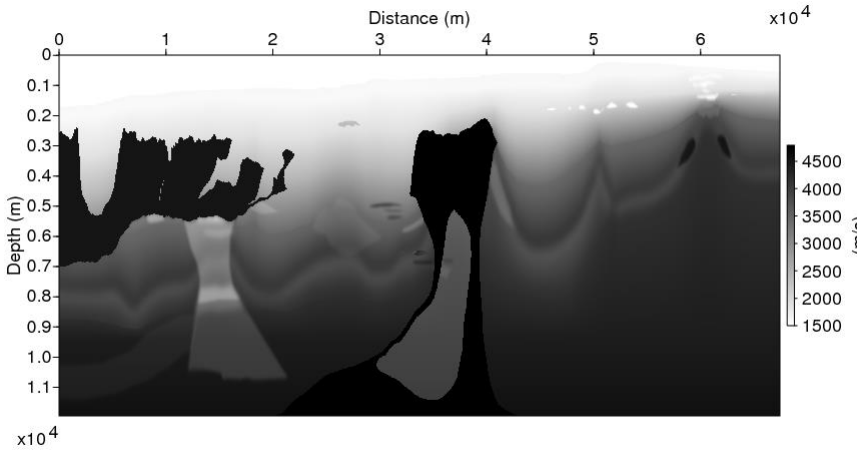

(a)

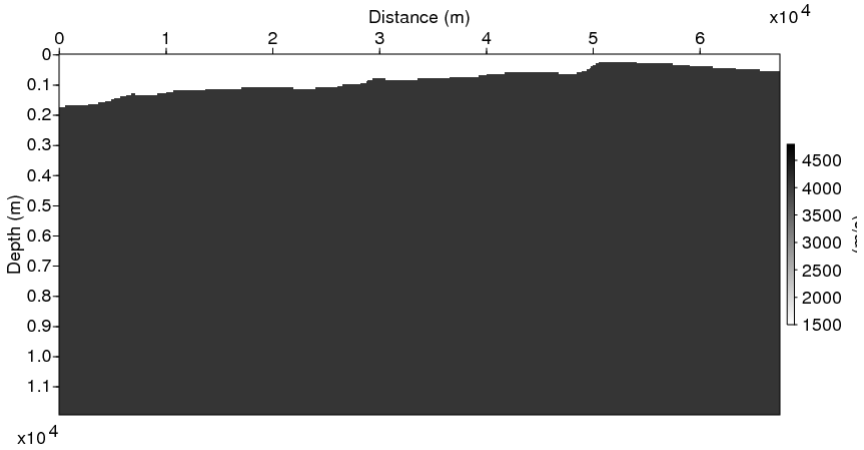

(b)

Figure 6 (a) The true BP P-wave velocity model and (b) the initial model with sea water velocity.

To investigate the suppression of the crosstalk effect in the truncated Gauss-Newton method, we compared the model updates and the inverted velocity models obtained by the truncated Gauss-Newton and the gradient descent methods using a Laplace constant of σ=1. Figure 7(a) and 7(b) show the parameter updates from the truncated Gauss-Newton method and the gradient descent method, respectively. While a salt dome shape similar to that in Figure 6(a) was detected in the updates of the truncated Gauss-Newton method (Figure 7(a)), this shape was blurred downward in the updates of the gradient descent method (Figure 7(b)). From these results, we can confirm that consideration of the Hessian matrix suppresses the crosstalk effect.

Figure 8(a) and 8(b) show the velocity models obtained by using the truncated Gauss-Newton method and gradient descent method, respectively, with 5 Laplace constants: σ=1, 3, 5, 7, 9. The number of forward modeling used in the truncated Gauss-Newton method and the number of forward modeling used in the gradient descent method are equalized for a fair comparison. While the salt dome in the results of the gradient descent method is shifted downward (Figure 8(a)), the salt dome in the results of the truncated Gauss-Newton method is not (Figure 8(b)). The downward shift in the salt dome (Figure 8(a)) is the result of the distortion effect, which cannot be suppressed by the gradient descent method.

To compare the inaccuracy of model updates more precisely, we extracted depth profiles from the true BP benchmark model and the inverted velocity models (Figure 6(a), 8(a), and 8(b)). The depth profiles were extracted at a distance of 36,400 m from the left boundary, where a long salt dome is located. Two criteria in the depth profiles should be observed to compare how much they are influenced by the crosstalk effect. The first one is the downward shift in the upper boundary of the salt dome, which should be located at a depth of

2500 m. As the accuracy of the model updates decreases, the shallower parameters that have low velocities, ranging from 1500 m/s to 2000 m/s, will become blurred within the deeper area, which should contain a salt dome. This causes a downward shift in the upper boundary of the salt dome. The second criterion is the accuracy of the subsalt velocity below 5500 m. The accuracy of the subsalt velocity can deteriorate as the influence from the crosstalk effect becomes larger.

Figure 9 shows depth profiles of the true BP benchmark model (dashed line), velocity models inverted with the truncated Gauss-Newton method (solid line), and velocity models inverted with the gradient descent method (dotted line). Considering the two criteria, the truncated Gauss-Newton method matches the true model better than the gradient descent method in Figure 9. Therefore, the velocity model inverted using the truncated Gauss-Newton method was less influenced by crosstalk effect than the model inverted using the gradient descent method.

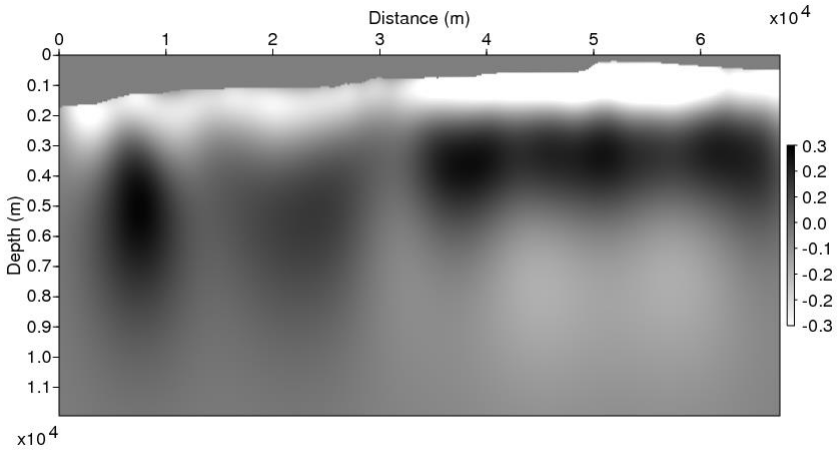

(a)

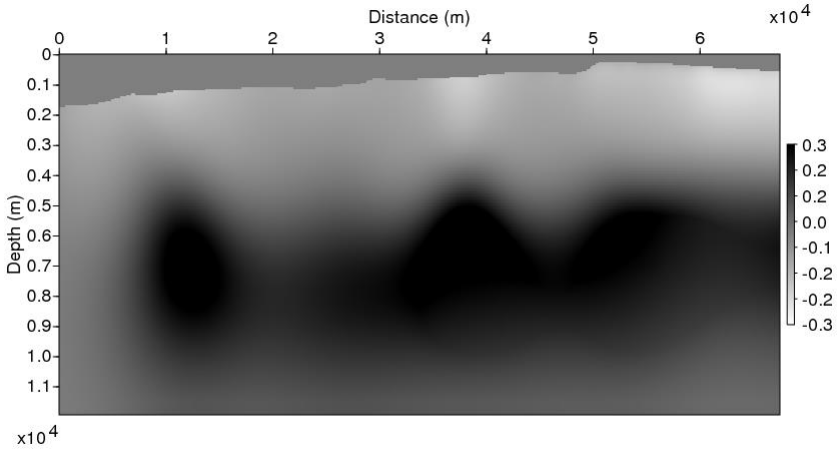

(b)

Figure 7 The first model updates of the BP benchmark model based on (a) the truncated Gauss-Newton method using a Laplace constant of σ=1 and (b) the gradient descent method using a Laplace constant of σ=1.

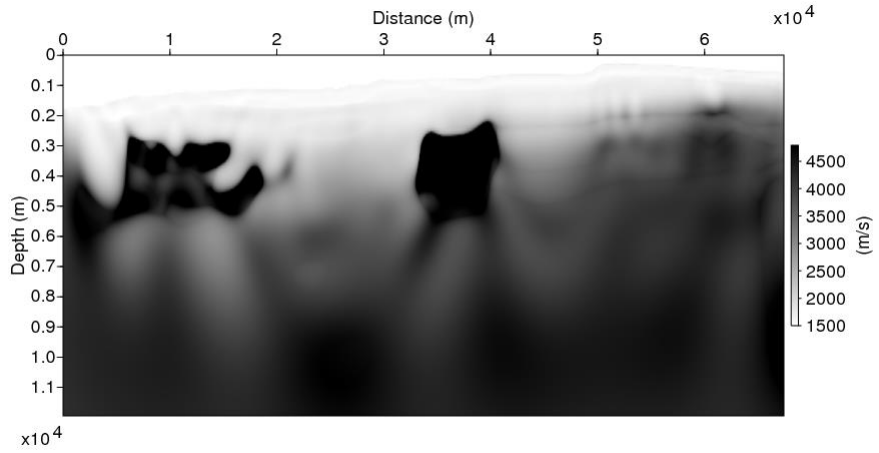

(a)

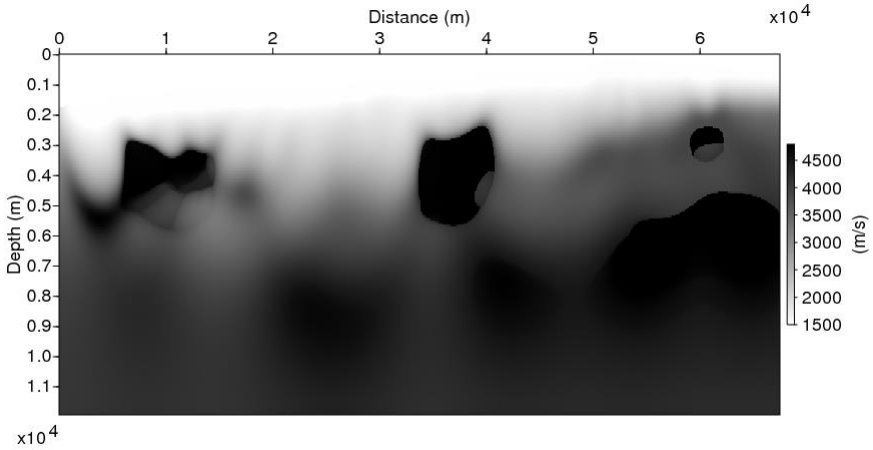

(b)

Figure 8 Inversion results of the BP benchmark model obtained using (a) the truncated Gauss-Newton method and (b) gradient descent method, respectively: the final inversion results obtained by using Laplace constants of σ=1, 3, 5, 7, 9.

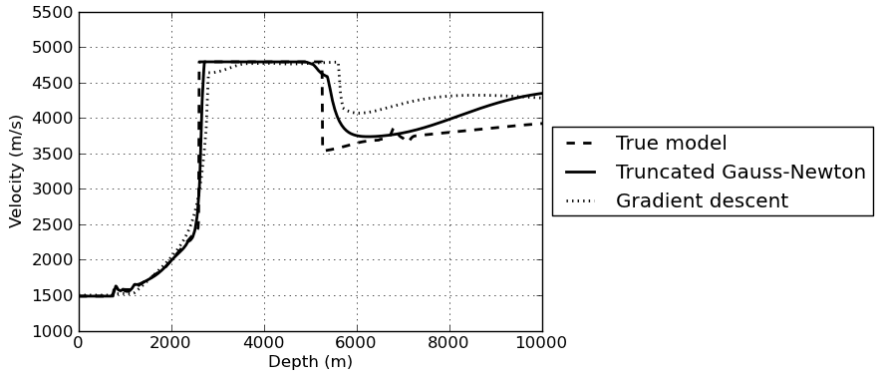

Figure 9 Depth profiles of the true BP benchmark model (dashed line, Figure 6(a)), velocity models inverted by the truncated Gauss-Newton method (solid line, Figure 8(a)), and velocity models inverted by the gradient descent method (dotted line, Figure 8(b)) with Laplace constants of [σ=1, 3, 5, 7, 9] at a distance of 36,650 m from the left boundary.

Chapter 4 Resolution analysis for Laplace-domain WI

It is well known that the model resolution of frequency-domain WI depends on the frequency bandwidth and the range of scattering angles (Wu and Toksöz 1987; Woodward 1992; Sirgue and Pratt, 2004). In this chapter, the model resolution of Laplace-domain WI is proved to be dependent on the Laplace constant bandwidth and the range of scattering angles similarly with frequency-domain WI. In the numerical example, we validate our analysis by observing the change in vertical and horizontal resolution depending on the offset-depth ratio and experimental setup.

4.1 Relationship between the number of attenuation constants and model resolution

It is clear that high-resolution models can be represented only when the number of model parameters M is large enough. Therefore, in order to obtain a high-resolution model, the Laplace-domain WI algorithm must have the ability to uniquely estimate as many model parameters as possible. In this section, we examine how many distinct attenuation constants should be used to determine M model parameters in an ideal case with no numerical error.

Model parameters can be estimated by Gauss-Newton method or gradient descent method as shown in Chapter 3. The model parameter vector estimated from the Gauss-Newton method can be expressed as follows:

$$\Delta p_{\mathbf{m}}^{est} = (L^T L + \epsilon I)^{-1} L^T \ln\left(\frac{d_{\mathbf{s},\mathbf{g}}(\sigma)}{u_{\mathbf{s},\mathbf{g}}(\sigma)}\right) \tag{4.1.1}$$

where ϵ is a damping factor. If ϵ is zero, we call Equation (4.1.1) the least squares solution. If ϵ is nonzero, we call Equation (4.1.1) the damped least squares solution.

The model parameter vector estimated from the gradient descent method can be given by:

$$\Delta p_{\mathbf{m}}^{est} = l L^T \ln\left(\frac{d_{\mathbf{s},\mathbf{g}}(\sigma)}{u_{\mathbf{s},\mathbf{g}}(\sigma)}\right). \tag{4.1.2}$$

where l is the step length. As shown in both cases, the estimated model parameter vector $\Delta p_{\mathbf{m}}^{est}$ is a linear combination of the exponential basis functions in both case. Data residuals $\ln\left(\frac{d_{\mathbf{s},\mathbf{g}}(\sigma)}{u_{\mathbf{s},\mathbf{g}}(\sigma)}\right)$ are the weights of the exponential basis functions in both cases shown in Equations (4.1.1) and (4.1.2).

For the exponential basis functions to span the Mth dimensional model space, the exponential basis functions should be linearly independent. If the number of elements in the set of linearly independent exponential basis functions increases, the exponential basis functions can span higher dimensional model space. Note that the set of the exponential basis functions whose attenuation constants are distinct is a linearly independent set. Thus, the number of distinct attenuation constants defines the maximum dimension of the estimated model space. This is directly related to the model resolution and whether the optimization method used is the gradient descent method or Gauss-Newton method.

From this, it can be seen that at least M distinct scattering attenuation numbers are required to determine the M model parameters uniquely. However, it has yet to be observed whether or not the M parameters can be completely determined by only a sufficient number of attenuation constants in a practical case with numerical errors. In the following section, we investigate the difficulties of stably and accurately determining the M model parameters with M distinct attenuation constants for the real case where numerical errors exist.

4.2 Relationship between the condition number of wavepath and model resolution

The previous section shows that the number of distinct attenuation constants is important for the uniqueness of estimated model parameters in the absence of numerical errors. Therefore, the model resolution is affected only by the number of distinct attenuation constants if there are no numerical errors. In practice, however, there are always numerical errors in the computation of estimated model parameters. The model resolution is influenced by these numerical errors. The measure of how the numerical error affects the problem is the condition number described in Chapter 3.2. In this section, we investigate how the condition number affects the model resolution in inverse problems.

First, we assume that model update $\Delta p_{\mathbf{m}}^{est}$ is estimated from the least squares with no damping factor ϵ (normal equation) which is shown as follows:

$$\Delta p_{\mathbf{m}}^{est} = (L^T L)^{-1} L^T \ln\left(\frac{d_{\mathbf{s},\mathbf{g}}(\sigma)}{u_{\mathbf{s},\mathbf{g}}(\sigma)}\right). \tag{4.2.1}$$

If $\Delta p_{\mathbf{m}}^{true}$ is the true model difference and we linearize the data residual vector as $\ln\left(\frac{d_{\mathbf{s},\mathbf{g}}(\sigma)}{u_{\mathbf{s},\mathbf{g}}(\sigma)}\right) \approx L\Delta p_{\mathbf{m}}^{true}$ and put this into Equation (4.2.1), we can obtain the following equation:

$$\Delta p_{\mathbf{m}}^{est} \approx (L^T L)^{-1} L^T L \Delta p_{\mathbf{m}}^{true}. \tag{4.2.2}$$

If the number of distinct attenuation constants is larger than the number of the model parameters and the $L^T L$ can be stably solved, the following equation is approximately true:

$$\Delta p_{\mathbf{m}}^{est} \approx \Delta p_{\mathbf{m}}^{true}. \tag{4.2.3}$$

This means the model parameters $\Delta p_{\mathbf{m}}^{est}$ can be perfectly resolved if the $L^T L$

can be stably solved.

Unfortunately, Equation (4.2.3) is scarcely solved with stability if the problem is ill-conditioned. According to Trefethen and Bau (1997), the relative error of the estimated model update $\Delta p_{\mathbf{m}}^{est}$ satisfies the following equation if the optimization algorithm is least squares without the damping factor ϵ:

$$\frac{\|\delta\Delta p_{\mathbf{m}}^{est}\|}{\|\Delta p_{\mathbf{m}}^{est}\|} = O(\kappa(L)^2\epsilon_{machine}), \tag{4.2.4}$$

where $\epsilon_{machine}$ is *machine epsilon* and is as large as the minimum value among the gaps between floating point numbers. As shown in Equation (4.2.4), the relative error of the estimated model update is governed by $\kappa(L)^2$, not $\kappa(L)$. If $\kappa(L)$ is large, $\frac{\|\delta\Delta p_{\mathbf{m}}^{est}\|}{\|\Delta p_{\mathbf{m}}^{est}\|}$ is extremely sensitive, even in the case of small numerical error. As shown in Chapter 3.2, it is confirmed that the condition number of the wavepath of the Laplace domain increases exponentially as the number of model parameters to be estimated, M, is larger. This shows that the least squares method without the damping factor ϵ, shown Equation (4.2.1), for Laplace-domain WI with a considerable M, is unstable even though the number of distinct attenuation constants is larger than the number of the model parameters.

From this reason, there is no choice but to use the damping factor ϵ shown in Equation (4.1.1) of the previous section for stabilizing the estimation of model updates. We call the optimization scheme using the damping factor ϵ the *damped least squares method*. Trefethen and Bau (1997) confirm that the damped least squares method guarantees stability if some ϵ satisfying the following equation is used:

$$\frac{\|\epsilon I\|}{\|L^T L\|} = O(\epsilon_{machine}). \tag{4.2.5}$$

Using this damped least squares method, Laplace-domain WI can estimate the model parameters stably regardless of the condition number.

In the damped least squares algorithm, the problem is model resolution. We may inquire about how the use of damped least squares affect the resolution of the estimated model parameters. If $\Delta p_{\mathbf{m}}^{true}$ is the true model difference and we linearize the data residual vector as $\ln\left(\frac{d_{\mathbf{s},\mathbf{g}}(\sigma)}{u_{\mathbf{s},\mathbf{g}}(\sigma)}\right) \approx L\Delta p_{\mathbf{m}}^{true}$ and put this into Equation (4.1.1), we can obtain the following equation:

$$\Delta p_{\mathbf{m}}^{est} \approx (L^T L + \epsilon I)^{-1} L^T L \Delta p_{\mathbf{m}}^{true}. \tag{4.2.6}$$

If we assume $R = (L^T L + \epsilon I)^{-1} L^T L$, then

$$\Delta p_{\mathbf{m}}^{est} \approx R\Delta p_{\mathbf{m}}^{true}. \tag{4.2.7}$$

We call R model resolution matrix as defined in Menke (2012). Note that R is never the unit matrix I, so $\Delta p_{\mathbf{m}}^{est} \neq \Delta p_{\mathbf{m}}^{true}$. This means the each component of $\Delta p_{\mathbf{m}}^{est}$ is the weighted average of components of $\Delta p_{\mathbf{m}}^{true}$, which weights of the components are the row of R. This means the model resolution is not perfect when the damped least squares is adopted.

We may then investigate how this model resolution affects the condition number of L. Let $\tilde{L}$ be a matrix satisfying $\tilde{L}^T\tilde{L} = L^T L + \epsilon I$. Here, the difference between $\tilde{L}$ and L represents the error of the data kernel caused by introduction of ϵ. Therefore, the following proposition is true:

$$\lim_{\tilde{L}\to L} R = I. \tag{4.2.8}$$

When an ϵ satisfying Equation (4.2.5) is introduced, the relative error between $\tilde{L}$ and L satisfies the following equation (Trefethen and Bau, 1997):

$$\frac{\left\|\tilde{L}-L\right\|}{\|L\|}=O(\kappa(L)^2\epsilon_{machine}). \tag{4.2.9}$$

From Equation (4.2.8) and Equation (4.2.9), we arrive at the conclusion that R moves away from I as the condition nubmer $\kappa(L)$ increases. This means that as the condition number of L increases, the resolution of the model estimated by damped least squares decreases.

In summary, the damped least squares method is numerically stable even with numerical errors but cannot provide perfect model resolution. This model resolution tends to be lower as the wavepath of the Laplace domain L becomes ill-conditioned. It is more serious if the number of model parameters M is considerable. However, M cannot be reduced because M limits the degree of freedom of the model. Therefore, for high model resolution, it is necessary to reduce the condition number as much as possible while keeping M large.

4.3 Range of the attenuation constants and condition number of data kernel matrix in the Laplace domain

In Chapter 3.2, we show that the Hessian of the Laplace domain is approximated to a real positive semidefinite Hankel matrix. In the previous section, for a high model resolution, we demonstrated a need for a method reducing the condition number as much as possible while keeping M sufficiently large. In this section, we show that the condition number decreases as the range of the attenuation constant increases. We also verify that the model resolution must be low if the range of the attenuation constant is small. Through this fact, we investigate the change of the condition number of the Hessian in the Laplace domain with respect to the range of the attenuation constant.

If $x = \exp(-\alpha\Delta z)$, we can express the Hessian matrix of the Laplace domain as the following Hankel matrix using Equation (3.2.8):

$$\begin{aligned} H_l(a,b,B) &= \left(h_{i+j}(a,b,B)\right)_{i,j=0,1,\cdots,n}, \\ h_k(a,b,B) &= \int_a^b B(\alpha)\exp(-\alpha k\Delta z)\,d\alpha, \end{aligned} \tag{4.3.1}$$

where a and b $(0 \le a \le b < \infty)$ are the lower and upper bound of the attenuation constant α, respectively. Beckermann (2000) studied how the condition number varies with this integration range $[a, b]$. According to Beckermann (2000), the following proposition is true:

$$\begin{aligned} [a,b] \supset [c,d] \rightarrow \inf\{\kappa(H_l(a,b,B)) : B(\alpha) \in \mathbb{R}\} \\ \le \inf\{\kappa(H_l(c,d,B)) : B(\alpha) \in \mathbb{R}\}, \end{aligned} \tag{4.3.2}$$

where $\mathbb{R}$ is the set of real numbers. This proposition implies that the condition number of the Hessian of the Laplace domain can increase as the range of the attenuation constant is limited. Since the condition number of the Hessian is the

square of the condition number of the wavepath, decrease of the integration range also means that the condition number of the wavepath in the Laplace domain increases. As shown in the previous section, this condition number of the Laplace-domain wavepath is inversely proportional to model resolution. Therefore, the proposition shown in Equation (4.3.2) suggests that the model parameter can be poorly resolved due to ill-conditioning if the range of attenuation constants is narrow.

As shown in Equation (2.4.11) of Chapter 2.4, the range of scattering attenuation constants is determined by the range of Laplace constants and incident angles. If the range of scattering angles or Laplace constants is limited, the range of attenuation constants will be limited, which in turn makes the inversion problem ill-conditioned. That is, the insufficient range of scattering angles or Laplace constants can be a main cause of low model resolution.

4.4 Numerical examples

Variation in resolution of by offset-depth ratio

As shown in Equation (2.4.11), the amplitude of the scattering attenuation constant vector of the wavepath $\boldsymbol{\alpha}$ is changed by the scattering (or incident) angle θ and Laplace constant σ as follows.

$$\boldsymbol{\alpha} \approx \frac{2\sigma}{c}\cos\left(\frac{\theta}{2}\right)\mathbf{n}. \tag{4.4.1}$$

This scattering angle is determined by the position of the source $\mathbf{s}$, the position of the receiver $\mathbf{g}$ and the target position $\mathbf{x}\,(=(x,y,z))$. Suppose a surface acquisition exploration in which sources and receivers exist only on the upper surface, such as marine seismic or land seismic. If the maximum offset is constant and position $\mathbf{x}$ is located deeper, the maximum value of the scattering angles becomes smaller. Also, when the depth of the target position is fixed, the maximum value of the scattering angles gradually increases as the maximum offset increases. If the reflective surface is horizontal and the position of the source receiver is parallel to the reflective surface, the relationship between the ratio of the maximum offset to the target depth and the maximum value of the scattering angles can be expressed by the following proportional expression.

$$\frac{\theta_{max}}{2} = \tan^{-1}\left(\frac{\max(|\mathbf{s}-\mathbf{g}|)}{2z}\right) = \tan^{-1}\left(R_{o/d}/2\right), \tag{4.4.2}$$

where $R_{o/d}$ is called *offset-depth ratio*, which represents the maximum offset divided by the target depth. If the source receiver is not parallel to a horizontal reflective surface, Equation (4.4.2) cannot be established. However, it is still valid in general that the larger the offset-depth ratio, the larger the maximum scattering angle is. Thus, as the offset-depth ratio increases, the maximum scattering angle increases and a wider range of scattering attenuation constants

becomes available. As we have seen in the previous section, a wider range of scattering attenuation constants provides higher model resolution. Therefore, we can reach a conclusion that the model parameters at the target depth has lower resolution as the target depth increases within the same offset.

This phenomenon has already been observed in Bae et al (2012) and Ha et al (2012). However, these studies provided little to no clarity on the cause of the relationship between offset-depth ratio and model resolution. This was due to a lack of understanding of the wavepath in the Laplace domain. In this paper, we have found that the offset-depth ratio affects the range of the scattering angles and the model resolution in Laplace-domain WI, similar to frequency-domain WI.

We examined how the resolution of a model inverted by Laplace-domain WI changes as the depth of a Gaussian, high-velocity anomaly increases to see how the model resolution varies with the offset-depth ratio.

Figure 10(a), Figure 11(a) and Figure 12(a) show the velocity models with anomalies whose depths are 0.75 km, 1.50 km, and 2.25 km, respectively. In this numerical example, the velocity model updates are estimated using the seismic data obtained in Figure 10(a), Figure 11(a) and Figure 12(a). We observe how their resolution change with the depth of the anomalies.

The maximum velocity of the Gaussian anomaly is 3.50 km/s and the background velocity is 1.70 km/s. The initial velocity model is a homogeneous velocity model with a velocity of 1.70 km/s. The size of the velocity model is 3 km x 6 km and the grid interval is 25 m. A fixed spread experiment was conducted for this test. The depth of both sources and receivers is 25 m and the maximum offset is 6 km. The interval of sources and receivers is 25m. The used Laplace constants range from 1.00 to 10.0 with an interval of 1.00.

Figure 10(b), Figure 11(b) and Figure 12(b) show the velocity model updates estimated using the seismic data obtained from Figure 10(a), Figure 11(a) and Figure 12(a) respectively. As shown in these figures, the resolution of the model update decreases as the depth of the target becomes deeper. This is because the range of scattering angles is limited as the depth increases. The limitation of the range of scattering angles appears both in the vertical scattering attenuation constant vector and in the nearly horizontal scattering attenuation constant vector reducing the vertical and horizontal resolution. From these numerical examples, we can confirm that the resolution of the model becomes poor as the target depth is increased.

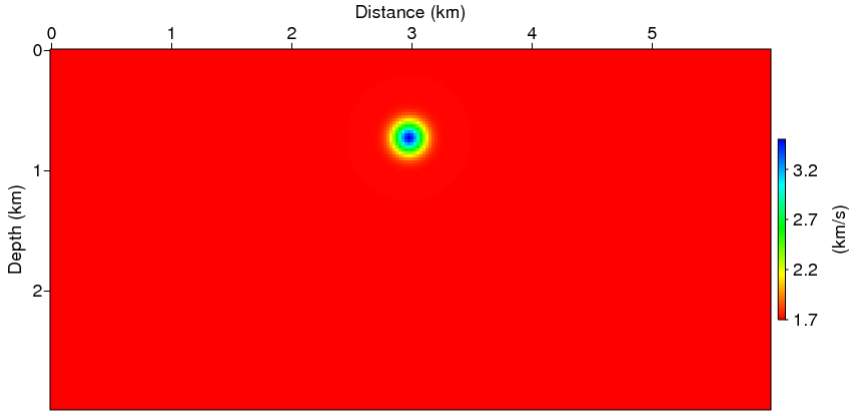

(a)

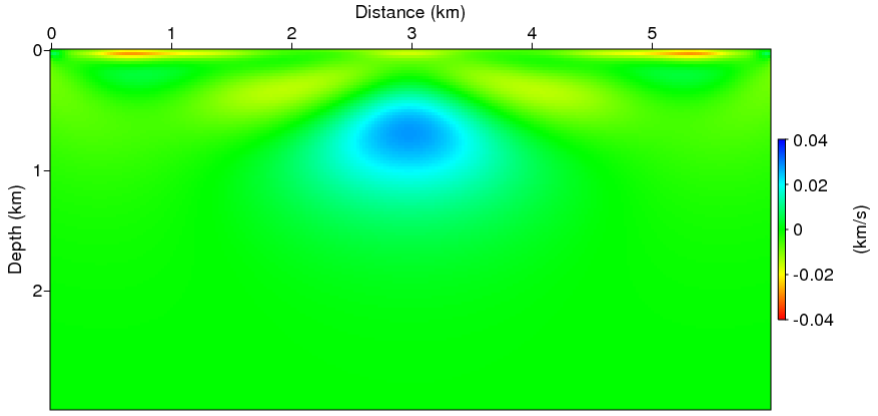

(b)

Figure 10 (a) True velocity model with a Gaussian anomaly of 3.50 km/s maximum velocity in a shallow region and (b) its estimated model update.

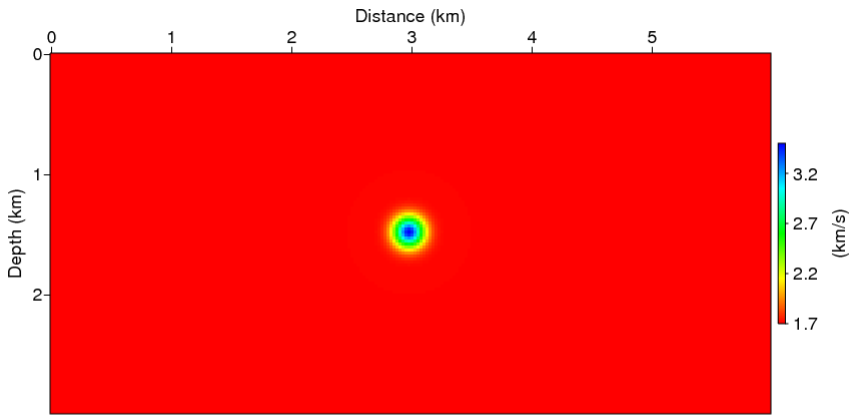

(a)

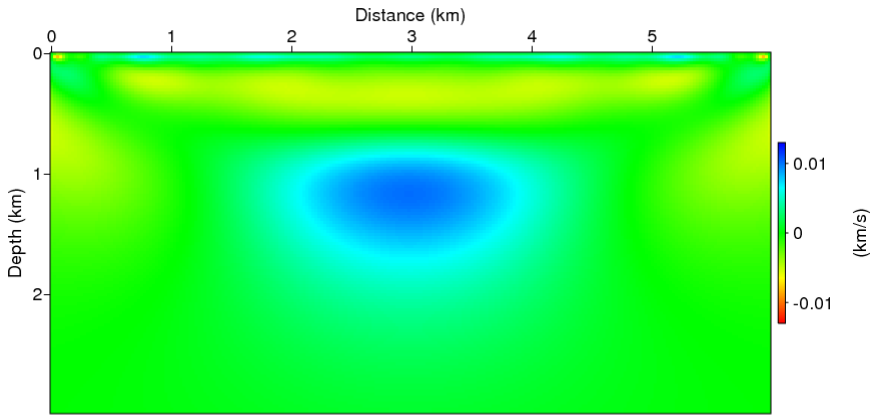

(b)

Figure 11 (a) True velocity model with a Gaussian anomaly of 3.50 km/s maximum velocity in the center and (b) its estimated model update.

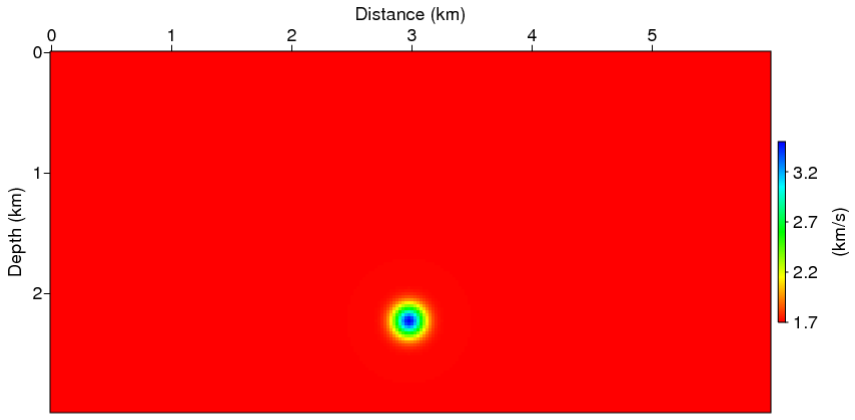

(a)

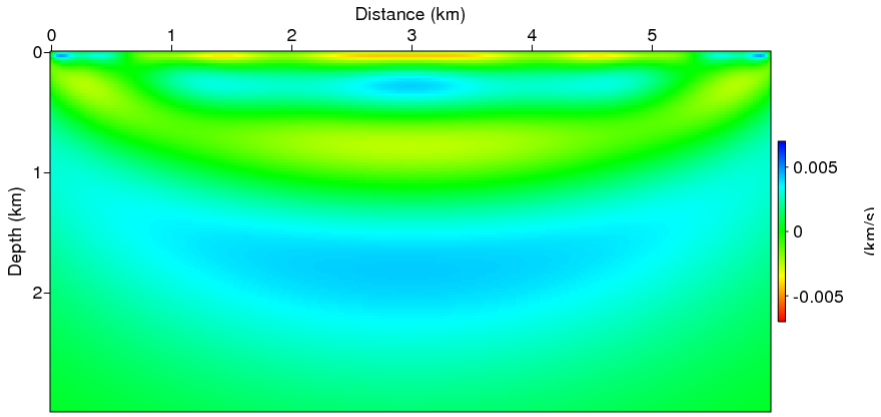

(b)

Figure 12 (a) True velocity model with a Gaussian anomaly of 3.50 km/s maximum velocity in a deep region and (b) its estimated model update.

Model resolution and types of experimental setup

There are many types of surface exploration in addition to surface experiments. This section investigates how the horizontal and vertical resolution of a model changes in surface reflection profiling (SRP), vertical seismic profiling (VSP) and cross-hole experiments similar to that performed by Virieux and Operto (2009). The experimental settings used in these tests are mostly similar to the experimental settings used in Figure 11 and differ only in the source-receiver positions. In the case of the SRP, the sources and receivers are all located along the top. In the case of the VSP, the sources are located along the top, the receivers along the left-side. Finally, in the case of the cross-hole experiment, the sources are located along the left-side, the receivers along the right-side.

As explained in Chapter 2, the relationship among the scattering attenuation constant, Laplace constant and incident angle in the Laplace domain corresponds exactly to the relationship among the scattering wavenumber, frequency and incident angle in the frequency domain. This similarity enables the analysis of spectral coverage in each experimental setup in the frequency domain to be applied to that of the Laplace domain. Devaney (1984) and Wu and Toksöz (1987) suggested the spectral coverage of the SRP data, VSP data and cross-hole data in the frequency domain. By using the analysis in the frequency domain, we can easily determine the coverage of scattering attenuation constants of each experimental setup as shown Figure 13.

Figure 13(a), (b) and (c) show the theoretical attenuation-constant coverage of the SRP data, VSP data and cross-hole data, respectively. By using the theoretical attenuation constant coverage, we can expect resolution change in any direction depending on the experimental setups.

All distances from the sources or receivers to the nearest boundary are 25m.

Both the interval of the sources and the interval of the receivers is 25m. In the case of the SRP, there are many attenuation constant vectors in the vertical direction and no attenuation constant vectors in the horizontal direction as shown in Figure 13(a). Therefore, the resolution in the horizontal direction is considerably worse than that in the vertical direction (Figure 14(b)).

On the other hand, in the case of the VSP, the range of the attenuation constant vectors whose directions are from top-left to bottom-right is wide and there is no attenuation constant vector whose direction is from top-right to bottom-left as shown in Figure 13(b). Therefore, the resolution from top-right to bottom-left is worse than the resolution from top-left to bottom-right (Figure 14(c)).

Finally, in the case of the cross-hole experiment, the range of the attenuation constant vectors in the vertical direction is wide and the vertical resolution is high as shown in Figure 13(c). Instead, the range of the attenuation constant vectors in the horizontal direction is limited to small values so the horizontal resolution is worse than the vertical resolution (Figure 14(d)).

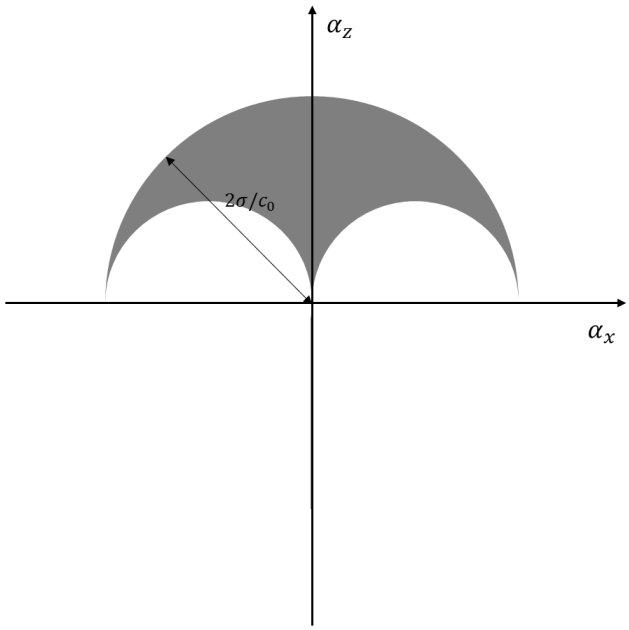
α_z
$2\sigma/c_0$
α_x

(a)

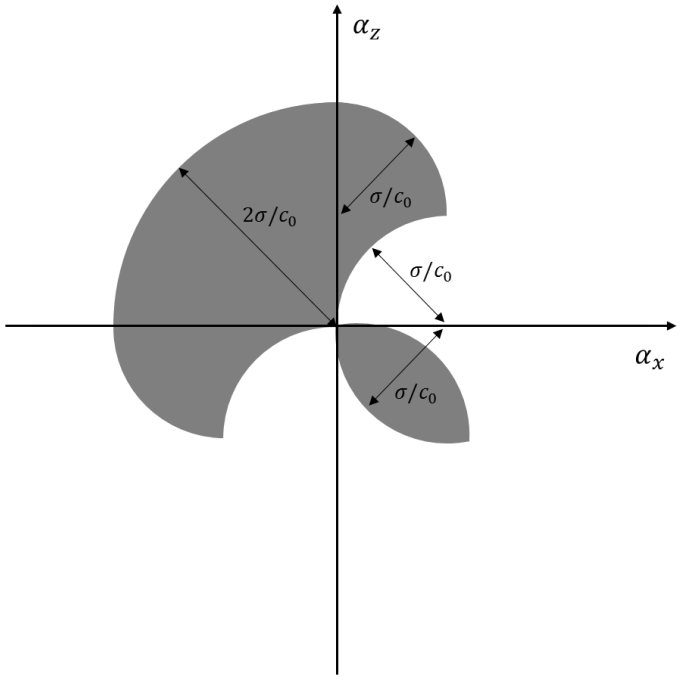
α_z
$2\sigma/c_0$
σ/c_0
σ/c_0
σ/c_0
α_x

(b)

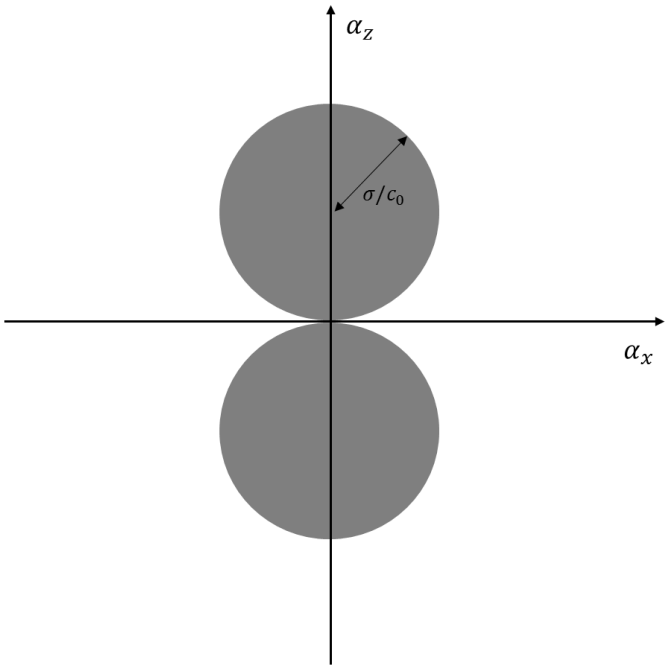

(c)

Figure 13 The coverages of scattering attenuation constants in the case of (a) the SRP data, (b) the VSP data and (c) the cross-hole data, where σ is the Laplace constant of the wavefield, and c_0 is velocity. $\boldsymbol{\alpha} = (\alpha_x, \alpha_z)$ is the 2D scattering attenuation constant vector.

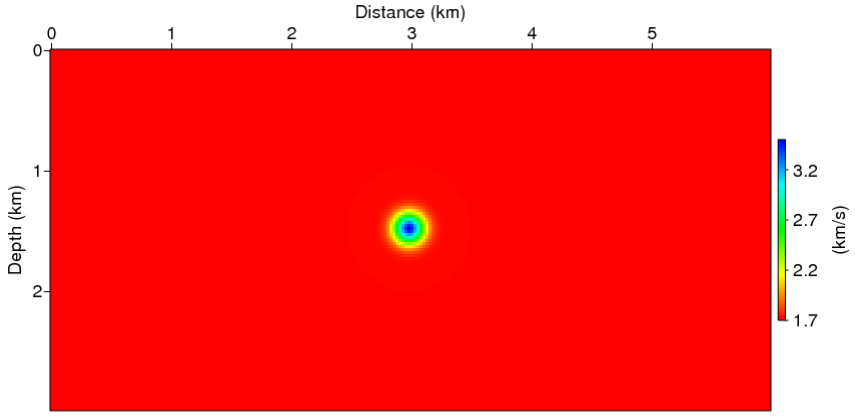
Distance (km)
0
1
2
3
4
5
Depth (km)
0
1
2
3.2
2.7
2.2
1.7
(km/s)

(a)

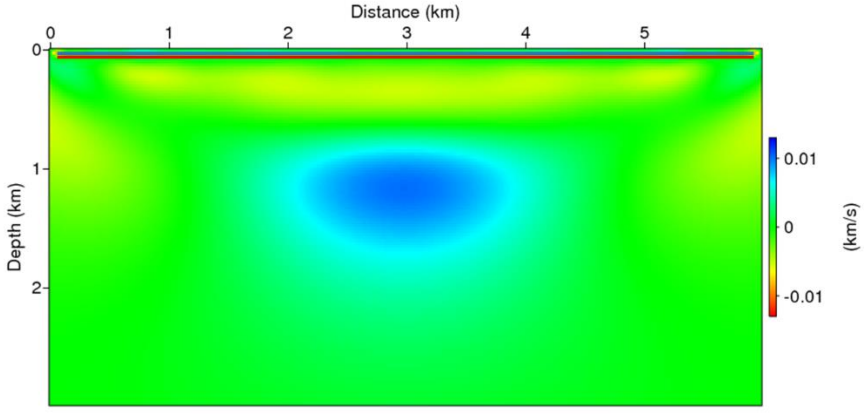
Distance (km)
0
1
2
3
4
5
Depth (km)
0
1
2
0.01
0
-0.01
(km/s)

(b)

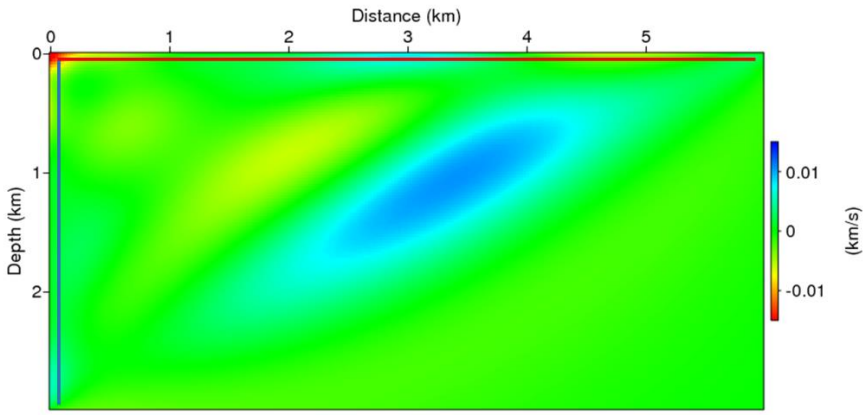

(c)

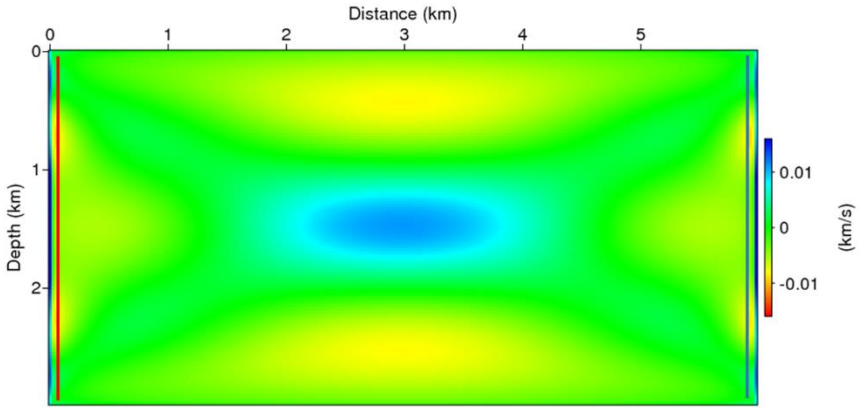

(d)

Figure 14 (a) The velocity model with a Gaussian, high-velocity anomaly, (b) the update of the model parameters in the SRP, (c) the update of the model parameters in the VSP and (c) the update of the model parameters in the cross-hole exploration environment. The red line indicates the location of the sources, and the blue line indicates the location of the receivers.

Chapter 5 An efficient strategy for Laplace constant selection

This chapter introduces a strategy for selecting a set of Laplace constants that keep the condition number reasonable while minimizing cost. We show that Laplace-domain WI is well-conditioned when it satisfies the conditions of continuity and minimum redundancy of attenuation constants. We also show how the Laplace constant should be chosen so that the vertical attenuation constant vector satisfies both conditions. To make the strategy more efficient, we further propose a modified method considering the geometrical spreading effect. We will also see if this strategy is valid even if the medium is 2D or 3D and heterogeneous.

5.1 Continuity and redundancy of attenuation constants

Park et al. (2010) has already proposed a method for reasonably determining the maximum and minimum values of the Laplace constant considering numerical error and depth penetration. Therefore, in this paper, we limit the discussion to how Laplace constants should be chosen between arbitrary upper and lower bounds of Laplace constants, but not how to determine the maximum or minimum of the Laplace constant. These minimum and maximum Laplace constants are assumed to be σ_1 and σ_{N_σ}, respectively, as defined in the previous section. Using Equation (2.4.11), the attenuation constant α can be restricted to the following maximum and minimum values:

$$\frac{2\sigma_1}{c_0} cos\theta_{max} = \alpha_{min} \leq \alpha \leq \alpha_{max} = \frac{2\sigma_{N_\sigma}}{c_0}, \qquad (5.1.1)$$

where θ is the scattering (or incident) angle and θ satisfies $0 \leq \theta \leq \theta_{max}$.

We should consider conditions of α which should be satisfied to make the inverse problem well-conditioned, without unreasonable cost, in the situation where α is bounded as in the above equation. If the sources and receivers are distributed densely enough near the top surface, the conditions that α should satisfy are:

1. *Continuity*

and

2. *Minimum redundancy.*

The following sections explain why these two conditions hold to make the inversion problem efficient and well-conditioned.

Continuity of attenuation constants

Suppose that there is an empty space in the range of α, as shown in Figure 15. The αs corresponding to this empty space are not parallel to other αs out of the empty space and can be sufficiently distinguished. The introduction of additional αs which are well distinct from other αs makes the problem more well-conditioned. Therefore, the presence of such an empty space in α means that linearly independent bases, which can help to effectively reduce the condition number of the inverse problem, are not used. Thus, the case where αs are filled between the minimum and maximum attenuation constants without empty sections is better-conditioned because it has more distinct bases than the case with empty sections. Therefore, it is preferred that the range of αs is continuous.

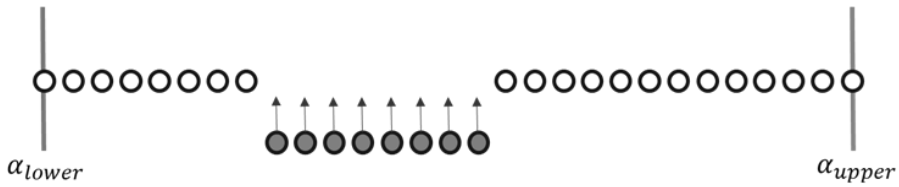

Figure 15 A diagram of attenuation constants illustrating the importance of continuity. The white circles represent attenuation constants with the empty sections that were originally present, and the gray circles represent attenuation constants that may be added to the empty section.

Less redundancy of attenuation constants

Suppose now that the attenuation constants are already set densely through the entire range. Now consider that additional Laplace constants may be introduced

as shown in Figure 16. This single additional Laplace constant generates additional attenuation constants within the range of existing attenuation constants. The attenuation constants generated by the newly introduced Laplace constant have values that are not significantly different from those existing. This means that the bases of the newly introduced Laplace constants are nearly dependent on the existing basis and do not contribute much to the reduction of the condition number. Therefore, the additional Laplace constants do not contribute to the improvement of model resolution.

The important thing to consider here is the additional costs of introducing new attenuation constants. Additional forward wavefield modeling processes are necessary for a new Laplace constant generating the new attenuation constants. Therefore, the addition of attenuation constants that overlap with the original range of attenuation constants is not an efficient choice because the degree of enhancement of the model update is insignificant compared to the additional cost required by it. In other words, overlapping ranges of attenuation constants created by different Laplace constants cause inefficiencies.

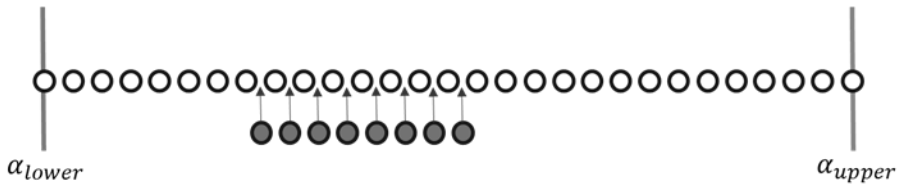

Figure 16 A diagram of attenuation constants illustrating the importance of minimum redundancy of attenuation constants. The white circles represent densely filled attenuation constants that were originally present, and the gray circles represent attenuation constants that may be added to the empty section.

5.2 An efficient strategy for Laplace constant selection

Our selection strategy is similar to the frequency selection strategy suggested by Sirgue and Pratt (2004) due to the similarity between the Green's functions in both the Laplace and frequency domain. Similarly to the frequency selection strategy, the purpose of the Laplace constant strategy is to make the vertical attenuation constants continuous and minimally redundant for all given source-receiver pairs and Laplace constants.

Given source-receiver pairs, the range of vertical attenuation constants of a single Laplace constant is defined. The vertical attenuation constant is at a maximum when the scattering angle is its smallest and the vertical attenuation constant is at a minimum when the scattering angle is at its largest. Therefore, we can express the maximum and minimum vertical attenuation constants of a single Laplace constant as follows:

$$\begin{aligned} \alpha_{i,max} &= \frac{2\sigma_i}{c_0}, \\ \alpha_{i,min} &= \frac{2\sigma_i}{c_0} cos\, \theta_{max}, \end{aligned} \tag{5.2.1}$$

where θ_{max} is the maximum angle at the depth of the target layer.

To make the vertical attenuation constants continuous, the maximum vertical attenuation constant of the ith Laplace constant should be equal to or larger than the minimum vertical attenuation constant of the $i+1$th Laplace constant. Also, to make the vertical attenuation constants have minimum redundancy, the maximum vertical attenuation constant of the ith Laplace constant should be equal to or smaller than the minimum vertical attenuation constant of the $i+1$th Laplace constant. To satisfy these two conditions (continuity and minimum

redundancy), the maximum vertical attenuation constant of the ith Laplace constant should be equal to the minimum vertical attenuation constant of the $i+1$th Laplace constant:

$$\alpha_{i+1,min} = \alpha_{i,max}. \tag{5.2.2}$$

Using this condition, we can obtain a recurrence formula of Laplace constants for satisfying continuity and minimum redundancy:

$$\sigma_{i+1} = \frac{\sigma_i}{cos\,\theta_{max}}. \tag{5.2.3}$$

The suggested strategy allows us to choose Laplace constants which make the coverage of the vertical scattering attenuation constants continuous and minimize vertical attenuation constant redundancy. From equation (5.2.3), we can confirm that larger of offset-depth ratios, require fewer Laplace constants in Laplace-domain WI. This property is similar with frequency selection for frequency-domain WI.

Figure 17(a) and (b) show that the algorithm can be efficiently performed without overlapping scattering attenuation constants by selecting Laplace constants such that $\alpha_{i+1,min}$ and $\alpha_{i,max}$ are equal. Figure 17(a) and (b) show how the Laplace constants should be selected to satisfy the continuity condition and the minimum redundancy condition when the offset-depth ratio is large or small, respectively. Figure 17 shows that a larger the offset-depth ratio, sparser the Laplace constants can be selected.

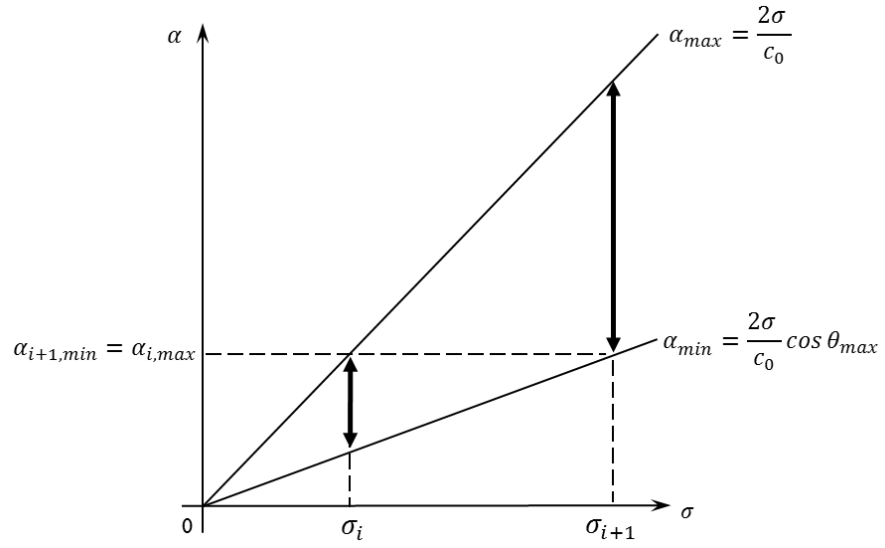

(a)

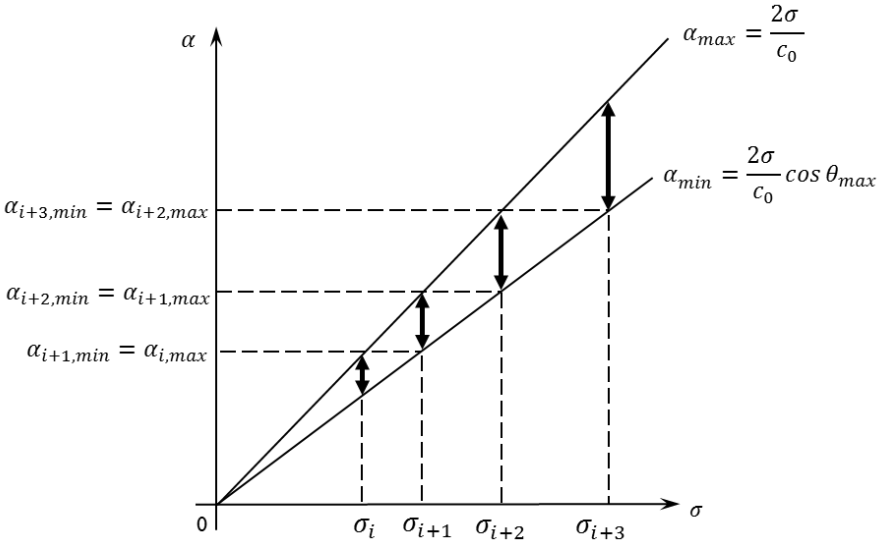

(b)

Figure 17 Illustration of the Laplace constant selection strategy. (a) and (b) show how the Laplace constants should be selected to satisfy the continuity condition and the minimum redundancy condition when the offset-depth ratio is large or small, respectively.

5.3 A modified Laplace constant selection strategy considering the geometrical spreading

As shown in Chapter 2.5, the geometrical spreading effect acts like an additional exponential term because the attenuation due to the geometrical spreading effect is hard to distinguish from the attenuation due to the Laplace constants in Laplace-domain WI. Therefore, if we do not consider the geometrical spreading effect as in Equation (5.2.3), the additional attenuation caused by geometrical spreading effect causes redundancy of basis. Therefore, considering the geometrical spreading effect, it is more reasonable to use a wider interval than the interval obtained from Equation (5.2.3). This section describes how to choose the Laplace constants considering the geometrical spreading effect in more detail.

According to Appendix A, the geometrical spreading effect can be approximately considered for the wavepath as follows. Generally, the Rytov wavepath of Laplace domain in 1D model case can be expressed as

$$L^{(nD)}(\mathbf{s},\mathbf{g},\mathbf{m},\sigma) \approx B^{(nD)}(\mathbf{s},\mathbf{g},\mathbf{o},\sigma)\exp\left(-\frac{2\sigma_{app}^{(nD)}}{c_0}cos\theta z\right), \quad (5.3.1)$$

where

$$\sigma_{app}^{(nD)} = \begin{cases} \sigma + \dfrac{c_0}{R} & if\ n = 3 \\ \sigma + \dfrac{c_0}{2R} & if\ n = 2 \\ \sigma & if\ n = 1 \end{cases}. \quad (5.3.2)$$

$\sigma_{app}^{(nD)}$ is the *n-dimensional apparent Laplace constant*. Substituting Equation (5.3.2) into Equation (5.2.3), we can obtain the relations of Laplace constants in 1D, 2D and 3D cases as:

$$\sigma_{i+1}^{(nD)} = \begin{cases} \dfrac{\sigma_i + \dfrac{c_0}{R_{min}}}{cos\,\theta_{max}} - \dfrac{c_0}{R_{max}} & if\ n = 3 \\ \dfrac{\sigma_i + \dfrac{c_0}{2R_{min}}}{cos\,\theta_{max}} - \dfrac{c_0}{2R_{max}} & if\ n = 2 \\ \dfrac{\sigma_i}{cos\,\theta_{max}} & if\ n = 1 \end{cases}, \tag{5.3.3}$$

where θ_{max} is the maximum angle at the depth of the target layer, and R_{min} and R_{max} are the shortest and longest distance from source (or receiver) to scattering point at the target layer, respectively. As shown in Equation (5.3.3), we can select the Laplace constants more sparsely due to the geometrical spreading effect in 2D and 3D cases. Figure 18 shows the Laplace-constant discretization strategy of 1D, 2D and 3D cases.

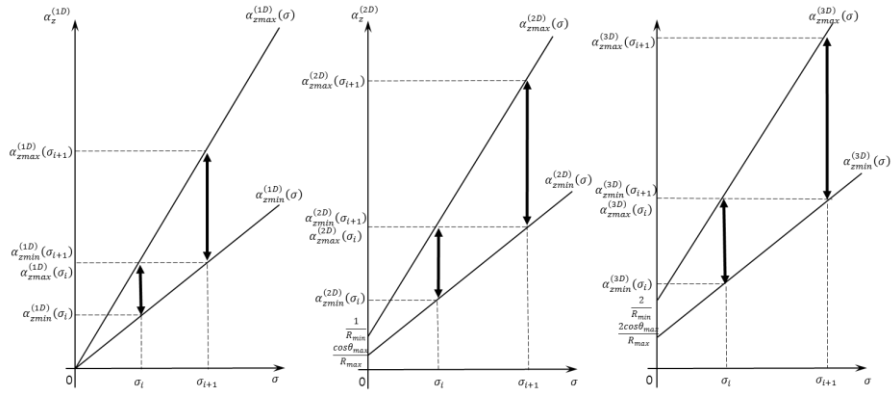

(a) (b) (c)

Figure 18 (a), (b), and (c) illustrate the Laplace constant selection strategy in one-, two-, and three-dimensions, respectively. A single Laplace constant produces a range of vertical attenuation constants of the wavepath, and Laplace constants are chosen such that the vertical attenuation constants are continuous and do not overlap across all ranges.

5.4 Effectiveness of the Laplace constant selection strategy in a 2D or 3D heterogeneous medium

The suggested strategy assumes that there are only straight rays in a homogeneous medium. The incident angles and the scattering angles also produce the vertical components of attenuation constant vector near the target. However, when we apply Laplace-domain WI to actual velocity models, we cannot make a 1D model assumption and a homogeneous analytic solution assumption. Therefore, the wave rays can be bent or non-perpendicular components can exist. As explained above, the nature of the attenuation constant vector of the wavepath in the Laplace domain shows large similarity with that of the wavenumber vector of the wavepath in the frequency domain. Due to its similarity, several changes of the attenuation constant vector of the wavepath in the Laplace domain are also similar to those of the wavenumber vector of the wavepath in the frequency domain, which are explained well in Sirgue and Pratt (2004). The validity of the Laplace constant selection strategy in the case of a 2D or 3D heterogeneous medium will be examined by comparing its similarity to the frequency selection strategy:

Existence of non-vertical attenuation constant vectors

In 2D or 3D heterogeneous models, the incident and scattering rays are not symmetric due to inclined reflective surfaces. Therefore, the inversion process generates non-vertical attenuation constant vectors as well as vertical attenuation constant vectors even though the Laplace constant selection strategy is derived with an assumption of 1D vertical models.

Ray bending

In the heterogeneous model, the ray bends due to wave refraction. In many cases, velocity increases with depth. The incident angle widens and the attenuation constant decreases. Extremely wide incident angles such as diving waves provide extremely low attenuation constants. The attenuation constant coverage of a single Laplace constant in this case is wider than the attenuation-constant coverage assuming a homogeneous model. Therefore, the application of the Laplace selection strategy can create some redundancy in the attenuation-constant coverage. Fortunately, the continuity of the attenuation-constant coverage can be preserved in this case.

Amplitude loss caused by reflections

In a heterogeneous medium, when wavefields meet the reflective surface, some are reflected and others are transmitted. This causes amplitude loss and changes the amplitude of the Laplace-domain wavepath. This amplitude loss does not change the attenuation constant vector in a local smooth area between reflective surfaces since. Amplitude loss occurs only at the reflective surface. That is, it has the effect of multiplying only constants to the wavepath. Therefore, the amplitude loss caused by reflections need not be considered in the Laplace constant selection strategy.

Difficulty of defining a representative velocity

If we consider the geometrical spreading effect, the representative velocity

needs to be considered in the Laplace constant selection strategy as shown in Equation (5.3.3). However, it is difficult to determine the representative velocity. If the representative velocity is set too high, there will be a problem with the continuity of attenuation constants. If the velocity is set too low, the redundancy of attenuation constants will increase. Satisfying the minimum redundancy of attenuation constants guarantees efficiency, while satisfying continuity ensures accuracy. Therefore, one has to choose between efficiency and accuracy. If accuracy is chosen as a priority, it is safe to set the representative velocity to the lowest expected velocity of the entire model. If efficiency is a priority, we recommend using the estimated average velocity of the entire model to the representative velocity.

We can confirm that the Laplace constant selection strategy is effective in maintaining the continuity of attenuation constants in 2D and 3D heterogeneous models considering only the representative velocity setting.

5.5 Numerical examples

Three-layered model

To verify the validity of the proposed Laplace constant selection strategy, we implement a comparison test with a 1D velocity model whose size is 10 km×3 km as shown in Figure 19. In this comparison test, inversion using the set of Laplace constants selected from the proposed strategy is compared to inversion using a set of Laplace constants with fixed intervals. The true velocity model is a three-layered model whose velocities are 1.7, 3.5 and 1.7 km/s from the top as shown in Figure 19. We use a homogeneous starting velocity model whose velocity is 1.7 km/s where the maximum offset is 10 km and the grid interval is 0.025 km. The fixed spread experiment was conducted for this test. The number of sources is 440 and the number of receivers is 440. The depth of sources and receivers is 25m. Both the interval of the sources and the interval of the receivers are 25m. In this test, we set the maximum depth, 3 km, as the depth of the target layer. We also fix the minimum and maximum Laplace constants as 1.0 s^{-1} and 10.0 s^{-1}, respectively.

Given the maximum offset (10 km) and the depth of the target layer (3 km), the cosine value of θ_{max} is 0.088, R_{min} is 3 km, and R_{max} is 5.83 km. Therefore, the set of Laplace constants (s^{-1}) selected by the suggested strategy is {1.000, 2.349, 4.970, 10.00}. The inversion using the set of Laplace constant is compared with the inversion using 8 sets of Laplace constants with fixed intervals as shown in Table 1. For Laplace-domain WI, we used the truncated Gauss-Newton method. After Laplace-domain WI was performed using the sets of Laplace constants in Table 1, the relative model misfit of each result was calculated using the following equation:

$$model\ misfit = \frac{1}{M_l}\left\|\frac{m_{inv} - m_{true}}{m_{true}}\right\|_1, \quad (5.5.1)$$

where m_{inv} is the inverted model parameter, m_{true} is the true model parameter and M_l is the number of model parameters on the vertical dotted line positioned at the center of the model. The first test was performed with 2500 iteration, which is expected to be sufficient for convergence. The relative model misfit of each result is shown in Table 2.

The relative model misfit of the results obtained from the proposed strategy is less than or equal to the relative model misfits of all the results obtained from the fixed interval strategy. The model misfit obtained by using the proposed Laplace constant selection strategy is less than or equal to the model misfit obtained through Laplace constants with a fixed interval, which is smaller than the smallest interval of the Laplace constant obtained through the proposed strategy. This implies that the proposed strategy for Laplace constants selection guarantees the continuity of the scattering attenuation constants and allows us to appropriately select the set of Laplace constants to such an extent that the exponential basis function sufficiently reflects the model.

The second test was performed with the same computational cost. This experiment compares the efficiency of each strategy shown in Table 1. It investigates whether or not the minimum redundancy of the scattering attenuation constant is guaranteed in each case. Because the number of modeling per iteration is set to the same, the computation cost of each strategy is equal if the product of the number of iterations and Laplace constants is constant. In this experiment, the product of the number of iterations and the number of Laplace constants is 5000 to compare the model misfit with the same calculation cost. The relative model misfit of each result is shown in Table 3.

The relative model misfit of the results obtained from the proposed strategy is much less than the relative model misfits of all the results obtained from the fixed interval strategy. This implies that the proposed strategy for Laplace constants selection guarantees the minimum redundancy of the scattering attenuation constants and allows us to perform the inversion process efficiently.

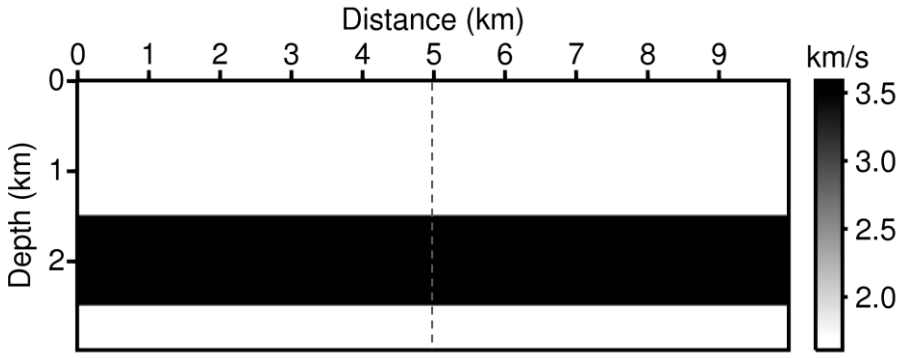

Figure 19 Three-layered velocity model. The relative model misfit of each inverted model parameter on the vertical dotted line is compared for this test.

Table 1 Description of the set of Laplace constants used in each strategy.

Strategy	Number of Laplace constants	Laplace constants (s^{-1})
Proposed strategy	4	1.000, 2.349, 4.970, 10.00
Fixed interval strategy (Conventional)	2	Range: 1.000 – 10.00, Interval: 9.000
	3	Range: 1.000 – 10.00, Interval: 4.500
	4	Range: 1.000 – 10.00, Interval: 3.000
	5	Range: 1.000 – 10.00, Interval: 2.250
	6	Range: 1.000 – 10.00, Interval: 1.800
	7	Range: 1.000 – 10.00, Interval: 1.500
	8	Range: 1.000 – 10.00, Interval: 1.286
	9	Range: 1.000 – 10.00, Interval: 1.125

Table 2 The relative model misfit of inverted model parameters obtained from each strategy with 2500 iterations, which is sufficient for convergence.

Strategy	Number of Laplace constants	Relative model misfit
Proposed strategy	4	3.059×10^{-2}
Fixed interval strategy (Conventional)	2	3.935×10^{-2}
	3	3.461×10^{-2}
	4	3.194×10^{-2}
	5	3.171×10^{-2}
	6	3.128×10^{-2}
	7	3.110×10^{-2}
	8	3.060×10^{-2}
	9	3.059×10^{-2}

Table 3 The relative model misfit of inverted model parameters obtained from each strategy with the same computational cost.

Strategy	Number of Laplace constants	Relative model misfit
Proposed strategy	4	3.440×10^{-2}
Fixed interval strategy (Conventional)	2	3.950×10^{-2}
	3	3.729×10^{-2}
	4	3.636×10^{-2}
	5	3.665×10^{-2}
	6	3.684×10^{-2}
	7	3.724×10^{-2}
	8	3.758×10^{-2}
	9	3.816×10^{-2}

SEG/EAGE Salt dome model

The validity of the proposed Laplace constant selection strategy in 1D model cases was verified by the previous test using the three-layered velocity model. To verify the validity of the proposed Laplace constant selection strategy in a complex velocity model case, we also implement a comparison test with the SEG/EAGE salt dome model shown in Figure 20(a). In this comparison test, the results inverted with the set of Laplace constants selected from the proposed strategy is compared to two results inverted with the sets of Laplace constants selected sparsely or densely with fixed intervals.

The seismic data was generated using the 6th order finite-difference method (FDM) in the frequency domain. The fixed spread experiment was conducted for this test. The number of sources and receivers is 779. The maximum offset is 15.56 km. The depth and interval of sources and receivers is 20m. A 1D model, whose velocity increases from 1679m/s at the top to 3000m/s at the bottom, was used as an initial model for the Laplace-domain WI test (Figure 20(b)). We constrained the maximum velocity to 4450 m/s and the minimum velocity to 1679 m/s. In this test, we set the maximum depth, 4.180 km, as the depth of the target layer.

Given the maximum offset (15.56 km) and the depth of the target layer (4.180 km), the set of Laplace constants (s^{-1}) selected by the suggested strategy is $\{0.500, 1.063, 2.258, 4.798, 10.20\}$. The results inverted with the set of Laplace constants is compared with the results inverted with two sets of Laplace constants with fixed intervals as shown in Table 4. For Laplace-domain WI, we used the truncated Gauss-Newton method. After Laplace-domain WI was performed using the sets of Laplace constants in Table 4, the relative model misfit of each result was calculated using the following equation:

$$model\ misfit = \frac{1}{M}\left\|\frac{m_{inv} - m_{true}}{m_{true}}\right\|_1, \quad (5.5.2)$$

where m_{inv} is the inverted model parameter, m_{true} is the true model parameter and M is the number of model parameters.

The comparison test was performed with the same computational cost. This is an experiment that compares the efficiency of each strategy shown in Table 4. Because the total number of modellings per iteration constant, the computation cost of each strategy is equal if the product of the number of iterations and the number of Laplace constants is equal. In this experiment, the product of the number of iterations and the number of Laplace constants is set to 300 to compare the model misfit with the same calculation cost.

Figure 21(a) shows the velocity model inverted with Laplace constants selected by the proposed strategy. Figure 21(b) and (c) show the velocity models inverted with Laplace constants selected with sparse and dense intervals, respectively. As shown in Figure 21, the inverted result obtained from Laplace constants selected with the proposed strategy is closer to the true model (Figure 20(a)) than the results obtained from the two sets of Laplace constants selected at fixed intervals. It can be confirmed that the Laplace constants obtained from the proposed strategy can estimate low velocity zones below salt domes more accurately.

Figure 22 shows the model misfit of each velocity model obtained through each strategy depending on computational cost. As the inversion process proceeds, it can be seen that the velocity model obtained through the proposed Laplace constant selection strategy always shows a relatively low model misfit at the same calculation cost. It is confirmed that the use of the Laplace constants obtained from the proposed strategy is effective not only for the 1D model but

also for the complex model.

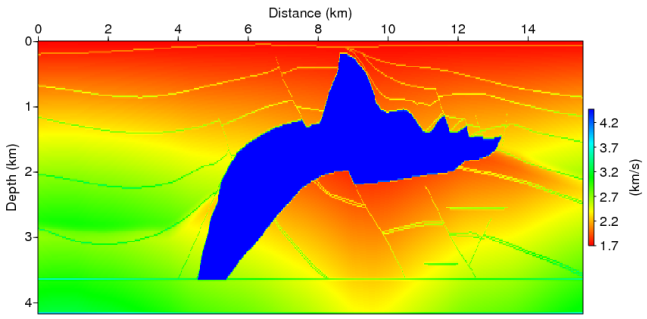

(a)

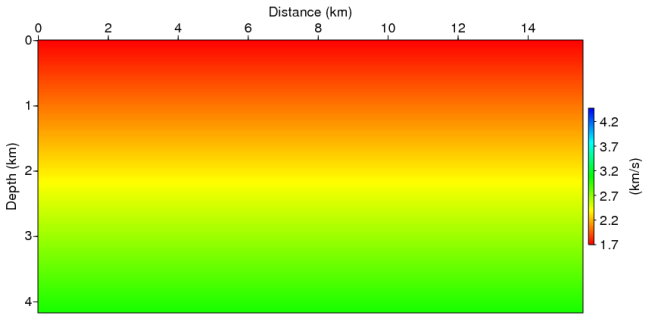

(b)

Figure 20 (a) The true SEG/EAGE Salt dome velocity model and (b) the initial model.

Table 4 Description of the set of Laplace constants used in each strategy.

Strategy	Number of Laplace constants	Laplace constants (s^{-1})
Proposed strategy	5	0.5000, 1.063, 2.258, 4.798, 10.20
Fixed interval strategy (Conventional)	3 (Sparse)	Range: 0.5000 – 10.20, Interval: 5.398
	19 (Dense)	Range: 0.5000 – 10.20, Interval: 0.5625

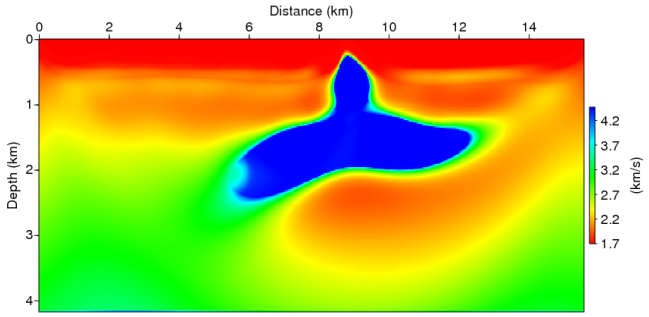

(a)

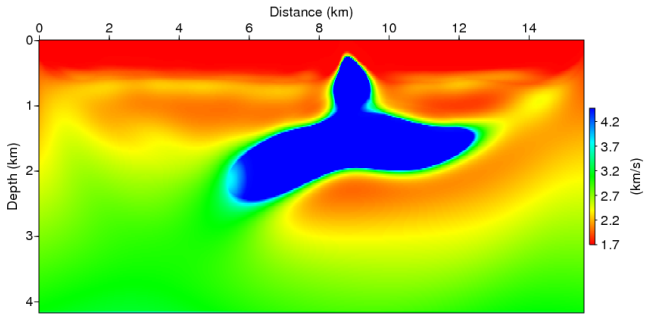

(b)

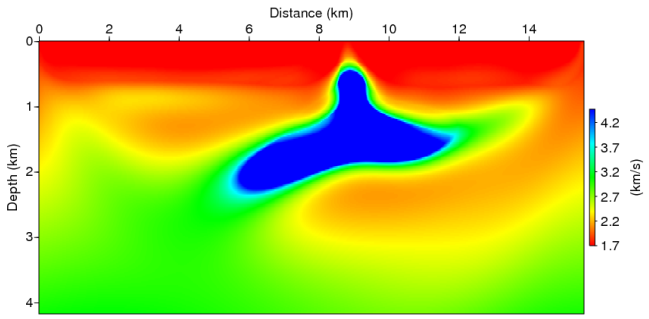

(c)

Figure 21 Inversion results of the BP benchmark model obtained using the set of Laplace constants selected with (a) the proposed strategy, (b) the conventional strategy with a sparse interval and (c) the conventional strategy with a dense interval.

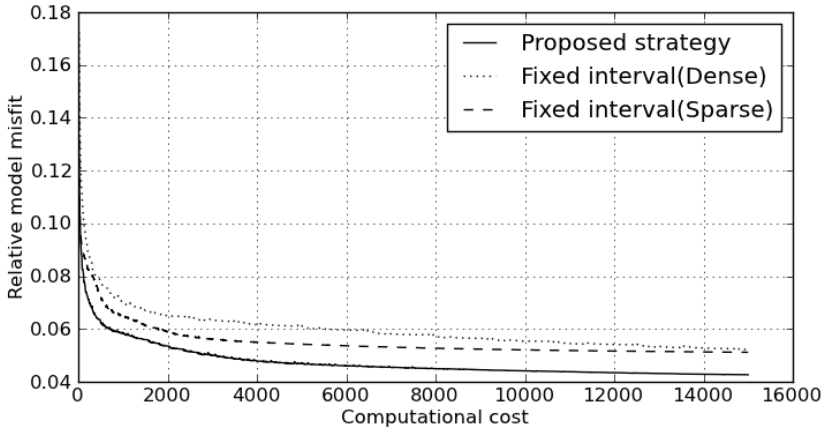

Figure 22 The relative model misfit of inverted model parameters obtained from each strategy depending on the product of the number of iterations and the number of Laplace constants, which represents the computational cost.

Chapter 6 Discussions & Conclusions

In this paper, we re-analyze the wavepath of the Laplace domain by introducing the concept of attenuation constants in the spatial domain. We prove that the Laplace-domain wavepath can be approximated to a real exponentially decaying basis, whose exponent is the product of the scattering attenuation constant vector and the space vector. It is also confirmed that the magnitude of the scattering attenuation constant vector is a function of the incident angle as well as the Laplace constant.

Several facts can be seen through the natures of the Laplace-domain wavepath. First, we can confirm that Laplace-domain WI is an ill-conditioned problem through the fact that the Laplace-domain wavepath is a real exponential decaying basis. We can confirm that the Gauss-Newton method should be used to obtain a satisfactory convergence rate. The truncated Gauss-Newton method using CG algorithm can be used as a solution to overcome the high-computational cost of the Gauss-Newton method. This requires a stopping criterion that detects the accuracy of locally quadratic approximations and prevents over-solving. The numerical example using the BP benchmark model shows that the truncated Gauss-Newton method plays a role in preventing distortion of the model update in Laplace-domain WI.

Second, the model resolution in the Laplace domain can be analyzed by introducing the concept of scattering attenuation constants. The range of attenuation constants affects the model resolution and scattering attenuation constant depends on the incident angle. These two facts make it possible to predict how model resolution varies with varying shot-receiver geometry and target positions. This analysis can explain the degradation of model resolution

as the depth is increased, which was observed in Bae et al. (2012) and Ha et al. (2012). Also, resolution change depending on the exploration environment can be explained as well. The incident-angle dependency of the model resolution of the Laplace domain is very similar to that of the frequency domain. This can be explained by the scattering attenuation constants of the Laplace domain, and the scattering wavenumbers of the frequency domain. Both affect the model resolution, are proportional to the cosine value of the incident angle.

Finally, the introduction of the concept of scattering attenuation constants can provide an efficient strategy for selecting the Laplace constants. This strategy is similar to the frequency selection strategy which was suggested by Sirgue and Pratt (2004). The Laplace constant selection strategy maintains the continuity of the range of attenuation constants for accuracy and minimizes the overlap of the range of attenuation constants for efficiency. Numerical examples show that the suggested Laplace constant selection strategy shows better accuracy and reduces cost compared to the conventional strategy.

This paper explains various features of Laplace-domain WI, such as ill-conditioning, scattering angle and the Laplace constant, which was not revealed in previous studies on Laplace-domain WI. Based on these analyses, we also present some new guidelines for Laplace-domain WI. This includes approaches such as the truncated Gauss-Newton method or the efficient Laplace-constant selection strategy. Moreover, this paper succeeded in raising the level of analysis of Laplace-domain WI to that of frequency-domain WI. Model resolution analysis was particularly highlighted by introducing a new concept called the attenuation constant corresponding to wavenumber. By demonstrating that the model resolution of Laplace-domain WI behaves similarly to frequency-domain WI, this paper suggests that the preceding studies on frequency-domain WI may be applied to Laplace-domain WI. In the

future, many techniques of frequency-domain WI are expected to be applied to Laplace-domain WI. In addition, this analysis for Laplace-domain WI is also expected to be applicable for other techniques using Laplace constants or complex frequencies.

Appendix A. Rytov wavepath considering the geometrical spreading

1D case

$$L^{(1D)}(\mathbf{s},\mathbf{g},\mathbf{m},\sigma) \approx \frac{\sigma^2}{g_0(\mathbf{g}|\mathbf{s},\sigma)} \frac{\exp\left(-\alpha\left(|\mathbf{r}_s| + |\mathbf{r}_\mathbf{g}|\right)\right)}{4\alpha^2} \exp(-\alpha(\hat{\mathbf{s}} + \hat{\mathbf{g}}) \cdot \mathbf{x}) \quad \text{(A.1)}$$

Incident and scattering angles are always same due to Snell's law. If θ is an incident angle or a scattering angle, we can express $(\hat{\mathbf{s}} + \hat{\mathbf{g}})$ as:

$$(\hat{\mathbf{s}} + \hat{\mathbf{g}}) = 2cos\theta\mathbf{n} \quad \text{(A.2)}$$

Therefore, we can replace $\alpha(\hat{\mathbf{s}} + \hat{\mathbf{g}})$ of Equation (A.1) with Equation (A.2) and $\alpha = \sigma/c_0$:

$$L^{(1D)}(\mathbf{s},\mathbf{g},\mathbf{m},\sigma) \approx \frac{\sigma^2}{g_0(\mathbf{g}|\mathbf{s},\sigma)} \frac{\exp\left(-\alpha\left(|\mathbf{r}_s| + |\mathbf{r}_\mathbf{g}|\right)\right)}{4\alpha^2} \exp\left(-\frac{2\sigma}{c_0} cos\theta\mathbf{n} \cdot \mathbf{x}\right) \quad \text{(A.3)}$$

2D case

$$
\begin{aligned}
& L^{(2D)}(\mathbf{s},\mathbf{g},\mathbf{m},\sigma) \\
& \approx \frac{\sigma^2}{g_0(\mathbf{g}|\mathbf{s},\sigma)} \frac{\exp\left(-\alpha\left(|\mathbf{r}_s|+|\mathbf{r}_\mathbf{g}|\right)\right)\exp(-\alpha(\hat{\mathbf{s}}+\hat{\mathbf{g}})\cdot\mathbf{x})}{\sqrt{8\pi\alpha(|\mathbf{r}_\mathbf{s}|+\hat{\mathbf{s}}\cdot\mathbf{x})}\sqrt{8\pi\alpha\left(|\mathbf{r}_\mathbf{g}|+\hat{\mathbf{g}}\cdot\mathbf{x}\right)}} \\
& \approx \frac{\sigma^2}{g_0(\mathbf{g}|\mathbf{s},\sigma)} \frac{\exp\left(-\alpha\left(|\mathbf{r}_s|+|\mathbf{r}_\mathbf{g}|\right)\right)}{8\pi\alpha} \frac{\exp(-\alpha(\hat{\mathbf{s}}+\hat{\mathbf{g}})\cdot\mathbf{x})}{\sqrt{(|\mathbf{r}_\mathbf{s}|+\hat{\mathbf{s}}\cdot\mathbf{x})\left(|\mathbf{r}_\mathbf{g}|+\hat{\mathbf{g}}\cdot\mathbf{x}\right)}}
\end{aligned}
\tag{A.4}
$$

If $|\mathbf{x}| \ll |\mathbf{r}_\mathbf{s}|$ and $|\mathbf{x}| \ll |\mathbf{r}_\mathbf{g}|$ (far-field approximation)

$$
\begin{aligned}
& L^{(2D)}(\mathbf{s},\mathbf{g},\mathbf{m},\sigma) \\
& \approx \frac{\sigma^2}{g_0(\mathbf{g}|\mathbf{s},\sigma)} \frac{\exp\left(-\alpha\left(|\mathbf{r}_s|+|\mathbf{r}_\mathbf{g}|\right)\right)}{8\pi\alpha} \frac{\exp(-\alpha(\hat{\mathbf{s}}+\hat{\mathbf{g}})\cdot\mathbf{x})}{\sqrt{|\mathbf{r}_\mathbf{s}||\mathbf{r}_\mathbf{g}|+\left(|\mathbf{r}_\mathbf{g}|\hat{\mathbf{s}}+|\mathbf{r}_\mathbf{s}|\hat{\mathbf{g}}\right)\cdot\mathbf{x}}} \\
& \approx \frac{\sigma^2}{g_0(\mathbf{g}|\mathbf{s},\sigma)} \frac{\exp\left(-\alpha\left(|\mathbf{r}_s|+|\mathbf{r}_\mathbf{g}|\right)\right)}{8\pi\alpha\sqrt{|\mathbf{r}_\mathbf{s}||\mathbf{r}_\mathbf{g}|}} \frac{\exp(-\alpha(\hat{\mathbf{s}}+\hat{\mathbf{g}})\cdot\mathbf{x})}{\sqrt{1+\frac{|\mathbf{r}_\mathbf{g}|\hat{\mathbf{s}}+|\mathbf{r}_\mathbf{s}|\hat{\mathbf{g}}}{|\mathbf{r}_\mathbf{s}||\mathbf{r}_\mathbf{g}|}\cdot\mathbf{x}}}
\end{aligned}
\tag{A.5}
$$

If x is small, we can assume that $\frac{1}{\sqrt{1+2x}} = \exp(-x) + O(x^2)$. Since we assume $|\mathbf{x}| \ll |\mathbf{r}_\mathbf{s}|$ and $|\mathbf{x}| \ll |\mathbf{r}_\mathbf{g}|$, we can approximate Equation (A.5) as:

$$
\begin{aligned}
L^{(2D)}(\mathbf{s},\mathbf{g},\mathbf{m},\sigma) &\approx B^{(2D)}(\mathbf{s},\mathbf{g},\mathbf{o},\sigma)\ \exp\left(-\frac{|\mathbf{r}_\mathbf{g}|\hat{\mathbf{s}}+|\mathbf{r}_\mathbf{s}|\hat{\mathbf{g}}}{2|\mathbf{r}_\mathbf{s}||\mathbf{r}_\mathbf{g}|}\cdot\mathbf{x}\right)\exp(-\alpha(\hat{\mathbf{s}}+\hat{\mathbf{g}})\cdot\mathbf{x}) \\
&\approx B^{(2D)}(\mathbf{s},\mathbf{g},\mathbf{o},\sigma)\ \exp\left(-\left(\alpha(\hat{\mathbf{s}}+\hat{\mathbf{g}})+\frac{|\mathbf{r}_\mathbf{g}|\hat{\mathbf{s}}+|\mathbf{r}_\mathbf{s}|\hat{\mathbf{g}}}{2|\mathbf{r}_\mathbf{s}||\mathbf{r}_\mathbf{g}|}\right)\cdot\mathbf{x}\right) \\
&\approx B^{(2D)}(\mathbf{s},\mathbf{g},\mathbf{o},\sigma)\ \exp\left(-\left(\frac{2\sigma}{c_0}cos\theta\mathbf{n}+\frac{|\mathbf{r}_\mathbf{g}|\hat{\mathbf{s}}+|\mathbf{r}_\mathbf{s}|\hat{\mathbf{g}}}{2|\mathbf{r}_\mathbf{s}||\mathbf{r}_\mathbf{g}|}\right)\cdot\mathbf{x}\right)
\end{aligned}
\tag{A.6}
$$

3D case

$$L^{(3D)}(\mathbf{s},\mathbf{g},\mathbf{m},\sigma) \approx \frac{\sigma^2}{g_0(\mathbf{g}|\mathbf{s},\sigma)} \frac{\exp\left(-\alpha\left(|\mathbf{r_s}|+|\mathbf{r_g}|\right)\right)\exp(-\alpha(\hat{\mathbf{s}}+\hat{\mathbf{g}})\cdot\mathbf{x})}{16\pi^2(|\mathbf{r_s}|+\hat{\mathbf{s}}\cdot\mathbf{x})\left(|\mathbf{r_g}|+\hat{\mathbf{g}}\cdot\mathbf{x}\right)} \tag{A.7}$$

If $|\mathbf{x}| \ll |\mathbf{r_s}|$ and $|\mathbf{x}| \ll |\mathbf{r_g}|$ (far-field approximation)

$$\begin{aligned} & L^{(3D)}(\mathbf{s},\mathbf{g},\mathbf{m},\sigma) \\ & \approx \frac{\sigma^2}{g_0(\mathbf{g}|\mathbf{s},\sigma)} \frac{\exp\left(-\alpha\left(|\mathbf{r_s}|+|\mathbf{r_g}|\right)\right)}{16\pi^2} \frac{\exp(-\alpha(\hat{\mathbf{s}}+\hat{\mathbf{g}})\cdot\mathbf{x})}{|\mathbf{r_s}||\mathbf{r_g}|+\left(|\mathbf{r_g}|\hat{\mathbf{s}}+|\mathbf{r_s}|\hat{\mathbf{g}}\right)\cdot\mathbf{x}} \\ & \approx \frac{\sigma^2}{g_0(\mathbf{g}|\mathbf{s},\sigma)} \frac{\exp\left(-\alpha\left(|\mathbf{r_s}|+|\mathbf{r_g}|\right)\right)}{16\pi^2|\mathbf{r_s}||\mathbf{r_g}|} \frac{\exp(-\alpha(\hat{\mathbf{s}}+\hat{\mathbf{g}})\cdot\mathbf{x})}{1+\frac{|\mathbf{r_g}|\hat{\mathbf{s}}+|\mathbf{r_s}|\hat{\mathbf{g}}}{|\mathbf{r_s}||\mathbf{r_g}|}\cdot\mathbf{x}} \\ & \approx B^{(3D)}(\mathbf{s},\mathbf{g},\mathbf{o},\sigma)\ \frac{\exp(-\alpha(\hat{\mathbf{s}}+\hat{\mathbf{g}})\cdot\mathbf{x})}{1+\frac{|\mathbf{r_g}|\hat{\mathbf{s}}+|\mathbf{r_s}|\hat{\mathbf{g}}}{|\mathbf{r_s}||\mathbf{r_g}|}\cdot\mathbf{x}} \end{aligned} \tag{A.8}$$

If x is small, we can assume that $\frac{1}{1+x} = \exp(-x) + O(x^2)$. Since we assume $|\mathbf{x}| \ll |\mathbf{r_s}|$ and $|\mathbf{x}| \ll |\mathbf{r_g}|$, we can approximate Equation (A.8) as:

$$\begin{aligned} L^{(3D)}(\mathbf{s},\mathbf{g},\mathbf{m},\sigma) &\approx B^{(3D)}(\mathbf{s},\mathbf{g},\mathbf{o},\sigma)\ \exp\left(-\frac{|\mathbf{r_g}|\hat{\mathbf{s}}+|\mathbf{r_s}|\hat{\mathbf{g}}}{|\mathbf{r_s}||\mathbf{r_g}|}\cdot\mathbf{x}\right)\exp(-\alpha(\hat{\mathbf{s}}+\hat{\mathbf{g}})\cdot\mathbf{x}) \\ &\approx B^{(3D)}(\mathbf{s},\mathbf{g},\mathbf{o},\sigma)\ \exp\left(-\left(\alpha(\hat{\mathbf{s}}+\hat{\mathbf{g}})+\frac{|\mathbf{r_g}|\hat{\mathbf{s}}+|\mathbf{r_s}|\hat{\mathbf{g}}}{|\mathbf{r_s}||\mathbf{r_g}|}\right)\cdot\mathbf{x}\right) \\ &\approx B^{(3D)}(\mathbf{s},\mathbf{g},\mathbf{o},\sigma)\ \exp\left(-\left(\frac{2\sigma}{c_0}cos\theta\mathbf{n}+\frac{|\mathbf{r_g}|\hat{\mathbf{s}}+|\mathbf{r_s}|\hat{\mathbf{g}}}{|\mathbf{r_s}||\mathbf{r_g}|}\right)\cdot\mathbf{x}\right) \end{aligned} \tag{A.9}$$

For the 1D model, the incident angle and scattering angle are symmetric and the scattering attenuation constant vector can be written:

$$\boldsymbol{\alpha}_{app}^{(1D)}(\mathbf{s},\mathbf{g},\mathbf{o},\sigma) = (0,\frac{2\sigma}{c_0}\cos\theta)$$
$$|\mathbf{r_s}| = |\mathbf{r_g}| = R$$
$$\mathbf{n} = (0,1) \tag{A.10}$$
$$\mathbf{x} = (0,z)$$

Using Equation (A.10), we can obtain the wavepaths of the Laplace domain in 1D, 2D and 3D as follows:

1D case

$$\begin{aligned} L^{(1D)}(\mathbf{s},\mathbf{g},\mathbf{m},\sigma) &\approx B^{(1D)}(\mathbf{s},\mathbf{g},\mathbf{o},\sigma)\exp\left(-\frac{2\sigma}{c_0}cos\theta\mathbf{n}\cdot\mathbf{x}\right) \\ &\approx B^{(1D)}(\mathbf{s},\mathbf{g},\mathbf{o},\sigma)\exp\left(-\frac{2\sigma}{c_0}cos\theta z\right) \end{aligned} \tag{A.11}$$

2D case

$$\begin{aligned} &L^{(2D)}(\mathbf{s},\mathbf{g},\mathbf{m},\sigma) \\ &\quad\approx B^{(2D)}(\mathbf{s},\mathbf{g},\mathbf{o},\sigma)\ \exp\left(-\left(\frac{2\sigma}{c_0}cos\theta\mathbf{n}\right.\right. \\ &\quad\left.\left.+\frac{|\mathbf{r_g}|\hat{\mathbf{s}}+|\mathbf{r_s}|\hat{\mathbf{g}}}{2|\mathbf{r_s}||\mathbf{r_g}|}\right)\cdot\mathbf{x}\right) \\ &\approx B^{(2D)}(\mathbf{s},\mathbf{g},\mathbf{o},\sigma)\ \exp\left(-\left(\frac{2\sigma}{c_0}cos\theta\mathbf{n}+\frac{\hat{\mathbf{s}}+\hat{\mathbf{g}}}{2R}\right)\cdot\mathbf{x}\right) \\ &\approx B^{(2D)}(\mathbf{s},\mathbf{g},\mathbf{o},\sigma)\ \exp\left(-\left(\frac{2\sigma}{c_0}cos\theta\mathbf{n}+\frac{1}{R}cos\theta\mathbf{n}\right)\cdot\mathbf{x}\right) \\ &\approx B^{(2D)}(\mathbf{s},\mathbf{g},\mathbf{o},\sigma)\ \exp\left(-\frac{2}{c_0}\left(\sigma+\frac{c_0}{2R}\right)cos\theta z\right) \end{aligned} \tag{A.12}$$

3D case

$$
\begin{aligned}
&L^{(3D)}(\mathbf{s},\mathbf{g},\mathbf{m},\sigma) \\
&\qquad \approx B^{(3D)}(\mathbf{s},\mathbf{g},\mathbf{o},\sigma)\ \exp\left(-\left(\frac{2\sigma}{c_0}cos\theta\mathbf{n}\right.\right. \\
&\qquad \left.\left.+\frac{|\mathbf{r_g}|\hat{\mathbf{s}}+|\mathbf{r_s}|\hat{\mathbf{g}}}{|\mathbf{r_s}||\mathbf{r_g}|}\right)\cdot\mathbf{x}\right) \\
&\approx B^{(3D)}(\mathbf{s},\mathbf{g},\mathbf{o},\sigma)\ \exp\left(-\left(\frac{2\sigma}{c_0}cos\theta\mathbf{n}+\frac{\hat{\mathbf{s}}+\hat{\mathbf{g}}}{R}\right)\cdot\mathbf{x}\right) \\
&\approx B^{(3D)}(\mathbf{s},\mathbf{g},\mathbf{o},\sigma)\ \exp\left(-\left(\frac{2\sigma}{c_0}cos\theta\mathbf{n}+\frac{2}{R}cos\theta\mathbf{n}\right)\cdot\mathbf{x}\right) \\
&\approx B^{(3D)}(\mathbf{s},\mathbf{g},\mathbf{o},\sigma)\ \exp\left(-\frac{2}{c_0}\left(\sigma+\frac{c_0}{R}\right)cos\theta z\right)
\end{aligned}
\tag{A.13}
$$

Appendix B. Truncated Gauss-Newton method

Algorithm 1 shows the truncated Gauss-Newton method algorithm for FWI suggested by Métivier et al. (2013). The truncated Gauss-Newton method is based on the computation of the descent direction by the conjugate gradient (CG) algorithm. As shown in Algorithm 1, Laplace-domain wavefield, gradient, and Hessian-vector product should be computed in the truncated Gauss-Newton method algorithm. The Laplace-domain wavefield can be calculated using Equation (2.1.6). In this section, we explain how to calculate the gradient and Hessian-vector product.

Gradient computation

The gradient $\nabla E(p)$ can be expressed as follows:

$$\nabla E(p) = \sum_{\sigma} \sum_{s} \mathbf{L}(s,p,\sigma)^T \mathbf{r}(s,\sigma) \tag{B.1}$$

where $\mathbf{L}(s,p,\sigma)$ and $\mathbf{r}(s,\sigma)$ are the wavepath and residual vector, respectively. The Laplace-domain wavepath $\mathbf{L}(s,p,\sigma)$ can be expressed using the discretized impedance matrix $\mathbf{S}(\sigma)$:

$$\mathbf{L}(s,p,\sigma) = \mathbf{R}(s,\sigma)\mathbf{S}(\sigma)^{-1}\left[\frac{\partial \mathbf{S}(\sigma)}{\partial p}\mathbf{u}_{\mathrm{s}}(\sigma)\right] \tag{B.2}$$

where $\mathbf{R}(s,\sigma)$ is a mapping of the wavefield to the receiver locations including the weight which varies with the receiver locations. $\mathbf{r}(s,\sigma)$ and $\mathbf{R}(s,\sigma)$ depend on what objective function is used. By putting Equation (B.2) into (B.1), we can obtain the gradient formula

$$\nabla E(p) = \sum_{\sigma}\sum_{s}\left[\frac{\partial \mathbf{S}(\sigma)}{\partial p}\mathbf{u}_s(\sigma)\right]^T \mathbf{S}(\sigma)^{-1^T}\mathbf{R}(s,\sigma)^T\mathbf{r}(s,\sigma)$$
$$= \sum_{\sigma}\sum_{s}\left[\frac{\partial \mathbf{S}(\sigma)}{\partial p}\mathbf{u}_s(\sigma)\right]^T \boldsymbol{\lambda}_s(\sigma) \tag{B.3}$$

where

$$\mathbf{S}(\sigma)\boldsymbol{\lambda}_s(\sigma) = \mathbf{R}(s,\sigma)^T\mathbf{r}(s,\sigma). \tag{B.4}$$

$\boldsymbol{\lambda}_s(\sigma)$ is called the adjoint state. To obtain the gradient, we first solve Equation (2.1.6) for $\mathbf{u}_s(\sigma)$, Equation (B.4) for $\boldsymbol{\lambda}_s(\sigma)$, and finally calculate Equation (B.3) using $\mathbf{u}_s(\sigma)$ and $\boldsymbol{\lambda}_s(\sigma)$. Therefore, only two forward modelling processes for one shot-gather and a single Laplace constant are necessary to yield the gradient $\nabla E(p)$.

Hessian-vector product computation

The Hessian $\mathbf{H}(p)$ can be expressed as follows:

$$\mathbf{H}(p) = \sum_{\sigma}\sum_{s}\mathbf{L}(s,p,\sigma)^T\mathbf{L}(s,p,\sigma) \tag{B.5}$$

By putting Equation (B.2) into (B.5), we can obtain the Hessian-vector product:

$$\mathbf{H}(p)\mathbf{x} = \sum_{\sigma}\sum_{s}\left[\frac{\partial \mathbf{S}(\sigma)}{\partial p}\mathbf{u}_s(\sigma)\right]^T \mathbf{S}(\sigma)^{-1^T}\mathbf{R}(s,\sigma)^T\,\mathbf{R}(s,\sigma)\mathbf{S}(\sigma)^{-1}\left[\frac{\partial \mathbf{S}(\sigma)}{\partial p}\mathbf{u}_s(\sigma)\right]\mathbf{x}$$
$$= \sum_{\sigma}\sum_{s}\left[\frac{\partial \mathbf{S}(\sigma)}{\partial p}\mathbf{u}_s(\sigma)\right]^T \boldsymbol{\xi}_s(\sigma) \tag{B.6}$$

where

$$\mathbf{S}(\sigma)\boldsymbol{\xi}_s(\sigma) = \mathbf{R}(s,\sigma)^T\mathbf{R}(s,\sigma)\mathbf{S}(\sigma)^{-1}\boldsymbol{\alpha}_s(\sigma) \tag{B.7}$$

and

$$\mathbf{S}(\sigma)\boldsymbol{\alpha}_s(\sigma) = \left[\frac{\partial \mathbf{S}(\sigma)}{\partial p}\mathbf{u}_s(\sigma)\right]\mathbf{x}. \tag{B.8}$$

To obtain the Hessian-vector product, we first solve Equation (B.8) for $\boldsymbol{\alpha}_s(\sigma)$, Equation (B.7) for $\boldsymbol{\xi}_s(\sigma)$. And finally calculate Equation (B.6) using $\boldsymbol{\alpha}_s(\sigma)$ and $\boldsymbol{\xi}_s(\sigma)$. If the Laplace-domain wavefield $\mathbf{u}_s(\sigma)$ is stored in a computer's memory, it does not have to be recomputed. Thus, only two forward modelling processes for a single shot-gather and a single Laplace constant are necessary to yield the Hessian-vector product $\mathbf{H}(p)\mathbf{x}$.

Data: p_0, ϵ
Result: $\text{argmin}_p\ E(p)$
$p = p_0$
while $E(p) > \epsilon$ **do**
    compute Laplace domain wavefield u
    compute gradient $\nabla E(p)$
    set $\Delta p = 0$
    set $r = \nabla E(p)$
    set $x = -r$
    while $\|H(p)\Delta p + \nabla E(p)\| \leq \eta \|\nabla E(p)\|$ **do**
        Compute Hessian $-$ vector product $H(p)x$
        $\beta_1 = x^T H(p)x$
        if $\beta_1 \leq 0$ **then**
            stop the inner iterations
        else
            $\beta_2 = \|r\|^2$
            $\Delta p = \Delta p + (\beta_2/\beta_1)x$
            $r = r + (\beta_2/\beta_1)H(p)x$
            $x = -r + (\|r\|^2/\beta_2)x$
        end
    end
    $p = p + \gamma \Delta p$
end

Algorithm 1 Truncated Gauss-Newton method (Métivier et al., 2013)

References

Alkhalifah, T., & Choi, Y. (2012). Taming waveform inversion non-linearity through phase unwrapping of the model and objective functions. Geophysical Journal International, 191(3), 1171-1178.

Bae, H. S., Pyun, S., Shin, C., Marfurt, K. J., & Chung, W. (2012). Laplace domain waveform inversion versus refraction-traveltime tomography. Geophysical Journal International, 190(1), 595-606.

Beckermann, B. (2000). The condition number of real Vandermonde, Krylov and positive definite Hankel matrices. Numerische Mathematik, 85(4), 553-577.

Bharadwaj, P., Drijkoningen, G., & Mulder, W. A. (2013). Multi-objective full waveform inversion in the absence of low frequencies. In SEG Technical Program Expanded Abstracts 2013 (pp. 964-968). Society of Exploration Geophysicists.

Bozdağ, E., Trampert, J., & Tromp, J. (2011). Misfit functions for full waveform inversion based on instantaneous phase and envelope measurements. Geophysical Journal International, 185(2), 845-870.

Brenders, A. J., Charles, S., & Pratt, R. G. (2008, June). Velocity Estimation by Waveform Tomography in the Canadian Foothill-A Synthetic Benchmark Study. In 70th EAGE Conference and Exhibition incorporating SPE EUROPEC 2008.

Cai, W., & Qin, F. (1994). Three-dimensional refraction imaging. In SEG Technical Program Expanded Abstracts 1994 (pp. 629-632). Society of

Exploration Geophysicists.

Chen, J. B. (2014). Dispersion analysis of an average-derivative optimal scheme for Laplace-domain scalar wave equation. Geophysics, 79(2), T37-T42.

Chi, B., Dong, L., & Liu, Y. (2014). Full waveform inversion method using envelope objective function without low frequency data. Journal of Applied Geophysics, 109, 36-46.

Choi, Y., & Alkhalifah, T. (2013). Frequency-domain waveform inversion using the phase derivative. Geophysical Journal International, 195, 1904–1916.

Datta, D., & Sen, M. K. (2016). Estimating a starting model for full-waveform inversion using a global optimization method. Geophysics, 81(4), R211-R223.

Devaney, A. J. (1984). Geophysical diffraction tomography. IEEE Transactions on Geoscience and Remote Sensing, (1), 3-13.

Docherty, P. (1992). Solving for the thickness and velocity of the weathering layer using 2-D refraction tomography. Geophysics, 57(10), 1307-1318.

Eisenstat, S. C., & Walker, H. F. (1996). Choosing the forcing terms in an inexact Newton method. SIAM Journal on Scientific Computing, 17(1), 16-32.

Eisinberg, A., Franzè, G., & Salerno, N. (2001). Rectangular Vandermonde matrices on Chebyshev nodes. Linear Algebra and its Applications, 338(1-3), 27-36.

Fichtner, A., Trampert, J., Cupillard, P., Saygin, E., Taymaz, T., Capdeville, Y.,

& Villaseñor, A. (2013). Multiscale full waveform inversion. Geophysical Journal International, 194(1), 534-556.

Forgues, E., Scala, E., & Pratt, R. G. (1998). High resolution velocity model estimation from refraction and reflection data. SEG Technical Program Expanded Abstracts 1998 (pp. 1211-1214). Society of Exploration Geophysicists.

Golub, G. H., & Van Loan, C. F. (1996). Matrix computations. 1996. Johns Hopkins University, Press, Baltimore, MD, USA, 374-426.

Ha, W., Chung, W., Park, E., & Shin, C. (2012). 2-D acoustic Laplace-domain waveform inversion of marine field data. Geophysical Journal International, 190(1), 421-428.

Ha, W., & Shin, C. (2013). Why do Laplace-domain waveform inversions yield long-wavelength results?. Geophysics, 78(4), R167-R173.

Hampson, D., & Russell, B. (1984). First-break interpretation using generalized linear inversion. In SEG Technical Program Expanded Abstracts 1984 (pp. 532-534). Society of Exploration Geophysicists.

Hu, W., Abubakar, A., & Habashy, T. M. (2009). Simultaneous multifrequency inversion of full-waveform seismic data. Geophysics, 74(2), R1-R14.

Ikelle, L. T., & Amundsen, L. (2005). Introduction to petroleum seismology. Society of Exploration Geophysicists.

Jun, H., Kwon, J., Shin, C., Zhou, H., & Cogan, M. (2016). Regularized Laplace–Fourier-Domain Full Waveform Inversion Using a Weighted l2 Objective Function. Pure and Applied Geophysics, 1-26.

Kwon, J., Jin, H., Calandra, H., & Shin, C. (2016). Interrelation between

Laplace constants and the gradient distortion effect in Laplace-domain waveform inversion. *Geophysics*, *82*(2), R31-R47.

Liao, Q., & McMechan, G. A. (1996). Multifrequency viscoacoustic modeling and inversion. Geophysics, 61(5), 1371-1378.

Ma, Y., & Hale, D. (2013). Wave-equation reflection traveltime inversion with dynamic warping and full-waveform inversion. Geophysics.

Menke, W. (2012). Geophysical data analysis: Discrete inverse theory (Vol. 45). Academic press.

Métivier, L., Brossier, R., Virieux, J., & Operto, S. (2013). Full waveform inversion and the truncated Newton method. *SIAM Journal on Scientific Computing*, *35*(2), B401-B437.

Milinazzo, F., Zala, C., & Barrodale, I. (1987). On the rate of growth of condition numbers for convolution matrices. IEEE Transactions on Acoustics, Speech, and Signal Processing, 35(4), 471-475.

Park, E., Ha, W., Chung, W., Shin, C., & Min, D. J. (2013). 2D Laplace-domain waveform inversion of Field data using a power objective function. Pure and Applied Geophysics, 170(12), 2075-2085.

Park, S., Ha, W., Shin, C., Pyun, S., & Calandra, H. (2010). A strategy for selecting the Laplace damping constants in the Laplace-domain inversion: Based on relationship between the Laplace damping constant and the detectable depth of a high-velocity structure. In SEG Technical Program Expanded Abstracts 2010 (pp. 993-997). Society of Exploration Geophysicists.

Plessix, R. E., Michelet, S., Rynja, H., Kuehl, H., Perkins, C., de Maag, J. W.,

& Hatchell, P. (2010, June). Some 3D applications of full waveform inversion. In 72nd EAGE Conference and Exhibition-Workshops and Fieldtrips.

Pratt, R. G., Shin, C., & Hicks, G. J. (1998). Gauss-Newton and full Newton methods in frequency-space seismic waveform inversion. Geophysical Journal International, 133, 341–362.

Pratt, R. G., & Worthington, M. H. (1988). The application of diffraction tomography to cross-hole seismic data. Geophysics, 53(10), 1284-1294.

Press, W. H., Teukolsky, S. A., Vetterling, W. T., & Flannery, B. P. (1992). Numerical Recipes in C: The Art of Scientific Computing, 2nd Ed., Cambridge University Press, New York.

Pyun, S., Shin, C., Min, D. J., & Ha, T. (2005). Refraction traveltime tomography using damped monochromatic wavefield. Geophysics, 70(2), U1-U7.

Pyun, S., Son, W., & Shin, C. S. (2011). Implementation of the gauss-Newton method for frequency-domain full waveform inversion using a logarithmic objective function. Journal of Seismic Exploration, 20(2), 193.

Qin, F., Cai, W., & Schuster, G. T. (1993). Inversion and imaging of refraction data. In SEG Technical Program Expanded Abstracts 1993 (pp. 613-615). Society of Exploration Geophysicists.

Ratcliffe, A., Win, C., Vinje, V., Conroy, G., Warner, M., Umpleby, A., Stekl, I., Nangoo, T., & Bertrand, A. (2011). Full waveform inversion: A North Sea OBC case study. In SEG Technical Program Expanded Abstracts 2011 (pp. 2384-2388). Society of Exploration Geophysicists.

Sava, P., & Biondi, B. (2004a). Wave-equation migration velocity analysis. I. Theory. Geophysical Prospecting, 52(6), 593-606.

Sava, P., & Biondi, B. (2004b). Wave-equation migration velocity analysis. II. Subsalt imaging examples. Geophysical Prospecting, 52(6), 607-623.

Schneider, W. A., & Kuo, S. Y. (1985). Refraction modeling for static corrections. In SEG Technical Program Expanded Abstracts 1985 (pp. 295-299). Society of Exploration Geophysicists.

Shewchuk, J. R. (1994). An introduction to the conjugate gradient method without the agonizing pain.

Shin, C., & Cha, Y. H. (2008). Waveform inversion in the Laplace domain. Geophysical Journal International, 173(3), 922-931.

Shin, C., & Cha, Y. H. (2009). Waveform inversion in the Laplace—Fourier domain. Geophysical Journal International, 177(3), 1067-1079.

Shin, C., & Ha, W. (2008). A comparison between the behavior of objective functions for waveform inversion in the frequency and Laplace domains, Geophysics, 73(5), VE119–VE133.

Shin, C., Ko, S., Kim, W., Min, D. J., Yang, D., Marfurt, K. J., Shin, S., Yoon, K., & Yoon, C. H. (2003). Traveltime calculations from frequency-domain downward-continuation algorithms. Geophysics, 68(4), 1380-1388.

Shtivelman, V. (1996). Kinematic inversion of first arrivals of refracted waves—A combined approach. Geophysics, 61(2), 509-519.

Sirgue, L., Barkved, O. I., Van Gestel, J. P., Askim, O. J., & Kommedal, J. H. (2009, June). 3D waveform inversion on Valhall wide-azimuth OBC. In

71st EAGE Conference and Exhibition incorporating SPE EUROPEC 2009.

Sirgue, L., & Pratt, R. G. (2004). Efficient waveform inversion and imaging: A strategy for selecting temporal frequencies. Geophysics, 69(1), 231-248.

Stefani, J. P. (1995). Turning-ray tomography. Geophysics, 60(6), 1917-1929.

Strutz, T., (2016). Data Fitting and Uncertainty (A practical introduction to weighted least squares and beyond). 2nd edition, Springer Vieweg, ISBN 978-3-658-11455-8.

Tarantola, A. (1984). Inversion of seismic reflection data in the acoustic approximation. Geophysics, 49, 1259-1266.

Tarantola, A. (1986). A strategy for nonlinear elastic inversion of seismic reflection data. Geophysics, 51, 1893-1903.

Todd, J. (1954). The Condition Number of the Finite Segment of the Hilbert Matrix, Nat. Bur. of Standards Appl. Math. Series 39, 109–116.

Trefethen, L. N., & Bau III, D. (1997). Numerical linear algebra (Vol. 50). SIAM.

van Leeuwen, T., & Herrmann, F. J. (2013). Mitigating local minima in full-waveform inversion by expanding the search space. Geophysical Journal International, 195, 661-667.

Vigh, D., Jiao, K., Watts, D., & Sun, D. (2014). Elastic full-waveform inversion application using multicomponent measurements of seismic data collection. Geophysics, 79(2), R63-R77.

Virieux, J., & Operto, D. (2009). An overview of full-waveform inversion in

exploration geophysics. Geophysics, 74(6), WCC1–WCC26.

Warner, M., Ratcliffe, A., Nangoo, T., Morgan, J., Umpleby, A., Shah, N., Vinje, V., Štekl, I., Guasch, L., Win, C., Conroy, G., & Bertrand, A. (2013) Anisotropic 3D full-waveform inversion. Geophysics, 78(2), R59-R80.

Warner*, M., & Guasch, L. (2014). Adaptive waveform inversion: Theory. In SEG Technical Program Expanded Abstracts 2014 (pp. 1089-1093). Society of Exploration Geophysicists.

White, D. J. (1989). Two-dimensional seismic refraction tomography. Geophysical Journal International, 97(2), 223-245.

Wilkinson, J.H. (1965). The Algebraic Eigenvalue problem, Oxford: Clarendon Press.

Wright, S., & Nocedal, J. (1999). Numerical optimization. Springer Science, 35, 67-68.

Woodward, M. J. (1992). Wave-equation tomography. Geophysics, 57(1), 15-26.

Wu, R. S., & Toksöz, M. N. (1987). Diffraction tomography and multisource holography applied to seismic imaging. Geophysics, 52(1), 11-25.

Xu, S., Wang, D., Chen, F., Lambaré, G., & Zhang, Y. (2012). Inversion on reflected seismic wave. In SEG Technical Program Expanded Abstracts 2012 (pp. 1-7). Society of Exploration Geophysicists.

Zelt, C. A., & Barton, P. J. (1998). Three-dimensional seismic refraction tomography: A comparison of two methods applied to data from the Faeroe Basin. Journal of Geophysical Research: Solid Earth, 103(B4), 7187-7210.

Zhang, J., & Toksöz, M. N. (1998). Nonlinear refraction traveltime tomography. Geophysics, 63(5), 1726-1737.

Zhu, X., & McMechan, G. A. (1989). Estimation of a two-dimensional seismic compressional-wave velocity distribution by iterative tomographic imaging. International Journal of Imaging Systems and Technology, 1(1), 13-17.

초 록

라플라스 영역에서의 파동경로 분석과 이에 따른 파형역산의 전략

권 정 민

에너지시스템공학부

서울대학교 대학원

라플라스 영역 파형역산 알고리즘은 장파장 탄성파 속도 모델 추정 기술로서, 주파수 영역 및 시간 영역 파형역산과 같은 고해상도 속도 모델 추정 기술에 초기 속도 모델을 제공하는 용도로 사용된다. 주파수 영역 및 시간 영역 파형역산은 초기 속도 모델에 대단히 민감하기 때문에, 라플라스 영역 파형역산의 정확성은 전체 속도 모델 추정 과정에 있어서 대단히 중요한 요소이다. 또한 라플라스 파형역산에서 사용되는 라플라스 영역 파동장은 얻는 과정에서 많은 비용을 요구하기 때문에, 기술의 경제성 측면에서 라플라스 파형역산의 수렴속도 및 효율성은 역산 과정의 성패를 가르는 중요한 요소이다. 그러나 기존의 라플라스 파형역산에 대한 연구들에서는 모델 파라미터와 자료간의 관계를 나타내는 파동경로(wavepath)에 대한 고찰이 불충분한 관계로 모델 해상도 및 수렴속도 분석을 수행하는 데 어려움이 있었다. 본 연구는 기존의 연구에서 밝히지 못하였던 라플라스 영역의 파동경로의 성질을 규명하고, 이를 통해 기존의 연구에서 제대로

수행하지 못하였던 라플라스 영역 파형역산에 대한 수렴속도 및 모델 해상도, 그리고 효율성 분석을 수행한다. 먼저 공간 영역에 대한 라플라스 상수라 할 수 있는 감쇠 상수(attenuation constant)라는 개념을 도입함으로써 라플라스 영역의 파동경로가 근사적으로 감쇠 상수 벡터와 공간 벡터의 곱을 지수로 하는 실 지수함수 기저임을 증명한다. 이에 더하여 본 연구는 라플라스 영역의 파동 경로가 큰 조건수를 가지는 실 지수함수인 것을 통해, 빠른 수렴속도를 위해서는 라플라스 영역 파형역산에 가우스뉴턴법을 적용하는 것이 합리적임을 밝힌다. BP 벤치마크 모델의 수치 예제는 이러한 라플라스 영역 파형역산 알고리즘에서 가우스뉴턴법이 가지는 효용성을 증명해준다. 그리고 감쇠 상수 벡터가 라플라스 상수와 파의 입사 각도에 대한 함수임을 증명함으로써, 라플라스 영역 파형역산을 통해 높은 해상도의 모델을 얻기 위해서는 넓은 범위의 입사 각도가 필수적임을 밝힌다. 이러한 모델 해상도와 입사 각도 범위와의 관계는 오프셋-심도비(offset-depth ratio)가 증가함에 따라 모델 해상도가 낮아지는 이유를 설명해주며, 탐사환경에 따른 수평 및 수직 해상도의 변화 역시 예측할 수 있게 한다. 마지막 본 연구는 라플라스 영역 파형역산의 효율성을 향상시키는 방법으로 효율적인 라플라스 상수 선택 전략을 제안한다. 본 연구에서 제안하는 방법을 통해 선택된 라플라스 상수는 감쇠상수의 범위의 연속성을 유지시킴으로써 모델 해상도를 보장하며, 감쇠상수의 불필요한 중복을 최소화함으로써 효율성을 향상시킨다. 수치 예제로부터 제안된 라플라스 상수 선택 전략이 기존 연구에서 쓰여왔던 등간격으로 라플라스 상수 선택하는 전략에 비해 효율성 및

정확성의 두 가지 측면에서 월등한 결과를 산출해 내는 것을 확인할 수 있다.

주요어: 라플라스 영역 파형 역산, 파동경로, 가우스뉴턴법, 모델 해상도, 라플라스 상수 선택법

학번: 2013-21005